ACOUSTO-OPTICAL DEVICES

Acousto-optics broadly refers to the interactions between optical (light) waves and acoustic (sound) waves. In engineering, however, it is now common to refer to acousto-optics more narrowly as influences of the latter upon the former and various types of resulting devices of both scientific and technological importance. Significant influences are possible under certain situations because the refractive index grating created by acoustic waves will cause diffraction or refraction of an incident light wave. Acousto-optics is further branched into two subareas: bulk-wave and guided-wave acousto-optics. In the former both light and sound propagate as unguided (unconfined) columns of waves inside a medium. A great many studies in the area of bulk-wave acousto-optics since the 1960s have resulted in various types of bulk acousto-optical devices and subsystems (1–7). In the latter, both light and sound waves are confined to a small depth in a suitable solid substrate. This subarea has been a subject of considerable interest since the early 1970s (8–13) as an outgrowth of guided-optical wave (GOW) science and technology (14–20) and surface acoustic wave (SAW) device technology (21–24), which had undergone intensive research and development a few years earlier. The studies on guided-wave acousto-optics have generated many fruitful results. For example, the resulting wide-band planar guided-wave acousto-optical (AO) Bragg modulators and deflectors were widely used in the development and realization of micro-optical modules for real-time processing of radar signals, for example, integrated optic RF spectrum analyzers (13). More recently, integrated AO tunable filters have been actively explored for applications in wavelength-division-multiplex (WDM) fiber optic communication systems (25). This chapter presents a brief review of bulk-wave acousto-optics and a detailed treatment of guided-wave acousto-optics with emphasis on the principle of AO Bragg diffraction, the resulting wave-band optical modulators, deflectors and switches, RF signal processors and optical tunable filters, and their applications. It is important to stress that being free of mechanical moving parts is one of the unique advantages of AO devices.

In the section entitled "Bulk-Wave Acousto-optic Interactions," the geometry, working principles, and device characteristics of a basic bulk-wave AO Bragg modular together with its applications are summarized. It suffices to present a brief review on this subarea because a number of excellent review papers and chapters have been written. The basic configuration and mechanisms for planar guided-wave AO Bragg diffraction and the resulting diffraction efficiency and fre-

quency response are then analyzed in detail using the coupled-mode techniques in the section entitled "Guided-Wave Noncollinear Acousto-optic Interactions."

For convenience, the analysis is carried out for the simple but basic case involving a single-surface acoustic wave in a $LiNbO_3$ waveguide. The salient differences between guided-wave AO Bragg diffraction and bulk-wave AO Bragg diffraction are discussed. The key performance parameters of the resulting AO Bragg cell modulators and deflectors and their inherent limitations are then identified and discussed in the section entitled "Guided-Wave Noncollinear (Bragg) Acousto-optic Interaction." A comparison of the four major types of AO materials that have been studied is also given in the section entitled "Figure of Merit and Viable Substrate Materials." Extension of the coupled-mode technique to analysis of AO Bragg diffraction from multiple SAWs, namely, multiple tilted SAWs and phased SAWs, is briefly discussed. Also presented in the section entitled "Fabrication Technologies" are design, fabrication, testing, and measured performances of wide-band AO Bragg cells using Y-cut $LiNbO_3$ and Z-cut GaAs substrates. Some of the potential applications of wide-band guided-wave AO Bragg cells and modules in optical communications, computing, and RF signal processing are described in the section entitled "Integrated AO Device Modules and Applications." In the section entitled "Guided-Wave Collinear Acousto-optic Interactions," detailed coupled-mode analysis on guided-wave collinear AO interactions in $LiNbO_3$ with specific application to optical tunable filters is presented. Detailed filter performance characteristics at five practical optical wavelengths are provided together with a brief description of its application.

BULK-WAVE ACOUSTO-OPTIC INTERACTIONS

Characteristics of AO Bragg Diffraction Gratings in Isotropic Material

Figure 1 depicts the basic parameters of a moving active diffraction grating that may be created using the AO effects through bulk acoustic waves or SAW in appropriate material substrates and the physical quantities involved in Bragg diffraction of optical waves from such active gratings. The angle between the incident light and the diffraction grating can vary from 90° (Raman–Nath regime), Bragg angle (Bragg regime) to 180° or 0° (collinear regime). Raman–Nath diffraction consists of a number of side orders when the AO parameter $Q \equiv 2\pi\lambda_0 L/n\Lambda^2$ is less than or equal to 0.3, where λ_0, Λ, n, and L designate, respectively, the wavelength of the incident light (in free space), the periodicity of the grating, the refractive index of the medium, and the length of the grating (the interaction length). When the light wave is incident at the Bragg angle to be defined shortly and Q is larger than 4π, diffraction is of the Bragg type and consists of only one side order. The Bragg-type diffraction-based devices are capable of higher center carrier frequency, wider modulation bandwidth, larger dynamic range, and thus greater versatility in application.

Bragg diffraction requires that conservation of momentum and energy as expressed in Eqs. (1a, b) are simultaneously satisfied (1):

$$\boldsymbol{k}_d = \boldsymbol{k}_i \pm \boldsymbol{K} \tag{1a}$$

$$\omega_d = \omega_i \pm \omega_a \tag{1b}$$

where $\boldsymbol{k}_i$, $\boldsymbol{k}_d$, and $\boldsymbol{K}$ designate, respectively, the wave vector of the incident light, the diffracted light, and the acoustic wave, and ω_i, ω_d, and ω_a are their corresponding radian frequencies. Note that Eq. (1a) is also commonly called the phase-matching condition, and that in the case of an optically isotropic medium it reduces to the following well-known Bragg condition:

$$\lambda_0/n = 2\Lambda \sin\theta_B \tag{1c}$$

or

$$\theta_B = \sin^{-1}\left\{\frac{1}{2n}\left(\frac{\lambda_0}{\Lambda}\right)\right\} \tag{1d}$$

where λ_0, n, and Λ have been defined previously, and θ_B is the Bragg angle. Finally, the power of the Bragg-diffracted light I_D is given by the following simplified form:

$$I_D = I_i \sin^2\left(\frac{\omega_i}{2c}\Delta n L\right) \tag{1e}$$

where I_i, c, Δn, and L designate, respectively, the power of the incident light, the velocity of the light in free space, the peak changes in refractive index caused by the acoustic wave, and the interaction length. Δn depends upon the appropriate pho-

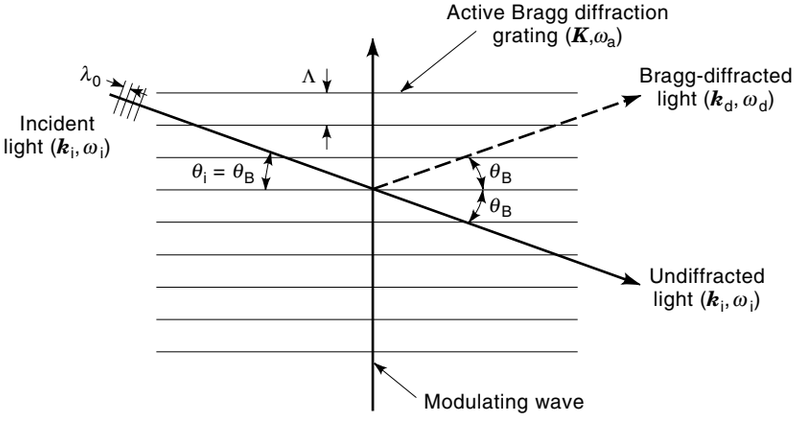

Figure 1. Configuration and parameters of moving active Bragg diffraction grating.

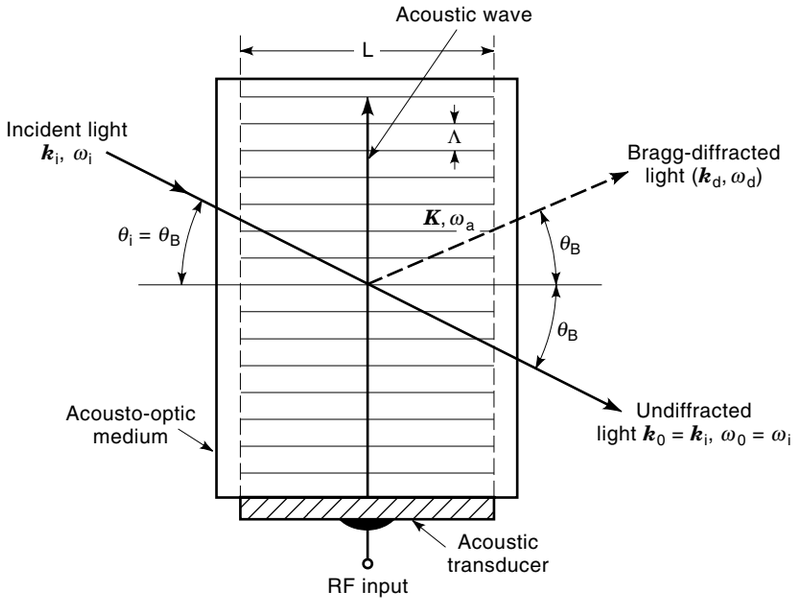

Figure 2. Basic bulk-wave acousto-optical Bragg cell modulator.

toelastic constants as well as the polarization and the propagation direction of the incident light, and the strength of the acoustic wave. It should be noted that when applied to guided-wave AO diffractions, which are treated later, Eq. (1e) will take a more complex form because the overlap integral between the guided-light waves and the SAW must be included.

The three characteristics of such active diffraction gratings upon which all types of AO Bragg devices follow.

1. The intensity of the Bragg-diffracted light can be controlled or modulated by the strength of the grating represented by the peak refractive index changes Δn, which is in turn determined by the propagation direction and polarization of both the light waves and the acoustic waves as well as the acoustic power. In general, the intensity of the diffracted light is proportional to the power of the acoustic wave before a certain nonlinear or saturation effect sets in. This characteristic is the basis for various types of AO intensity modulators.
2. For a given wavelength of the incident light, the direction of propagation of the diffracted light can be controlled by simultaneously varying the periodicity and the orientation of the grating. In a Bragg-type device the interaction length L is identical to the transducer aperture. Now, for a transducer aperture L, the angular beam spread (or wave vector spread) of the acoustic wave generated is roughly given by (Λ/L) in radian, where Λ again denotes the wavelength, which is also equal to the periodicity of the diffraction grating induced. Thus, for a given radio frequency (RF), the wave vector of a collimated incident light automatically finds a wave vector (and the corresponding diffraction grating) of appropriate orientation within the angular beam spread to satisfy the Bragg condition and undergo efficient Bragg diffraction. This characteristic is the basis for AO beam scanners and space switches.
3. The diffracted light carries a shift in frequency and in phase that are identical to that of the modulating acoustic wave. This last characteristic is the basis for AO frequency shifters and interferometric RF receivers.

Basic Bulk-Wave AO Bragg Cell Modulator

A basic bulk-wave AO Bragg cell modulator that is based on the acoustic diffraction grating just described is shown in Fig. 2. It consists of an acoustic cell of sufficiently large aperture and a laser source, both operating at suitable wavelengths. The acoustic cell is in turn made of a column of isotopic or anisotropic material that possesses desirable acoustic, optical, and AO properties. The acoustic waves are generated by applying an RF signal (at a frequency ranging from tens to thousands of megahertz) to a planar piezoelectric transducer that is bonded on one finely polished end face of the column. A Bragg diffraction grating is thus induced by the acoustic waves. In operation the input light is incident upon the diffraction grating at Bragg angle. The Bragg-diffracted output light propagates at an angle twice the Bragg angle from the incident (or undiffracted) light.

The brief analysis and results presented in the section entitled "Characteristic's of AO Bragg Diffraction Gratings in Isotropic Material" is exactly applicable to this basic optical modulator if the material involved is of the isotropic type. The analysis and results relevant to anisotopic material to be presented in the following section are more complicated (5,6).

Bulk-Wave AO Bragg Diffraction in Anisotropic Material

In the preceding discussion we have, for simplicity, considered bulk-wave AO Bragg diffraction in an optically isotropic material. However, because many superior AO materials are optically anisotropic, it is important to summarize the basic characteristics of anisotopic AO Bragg diffraction. Again for simplicity, we shall consider a specific configuration [shown in Fig. 3(a)] in which both the incident and the diffracted light

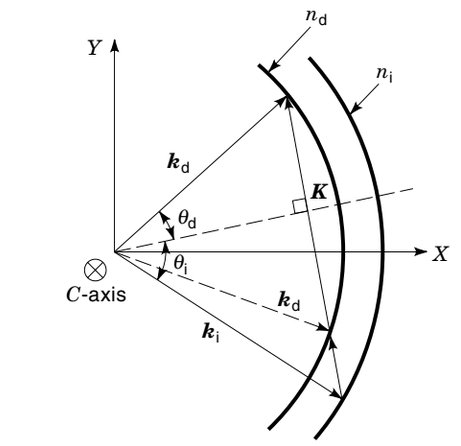

(a)

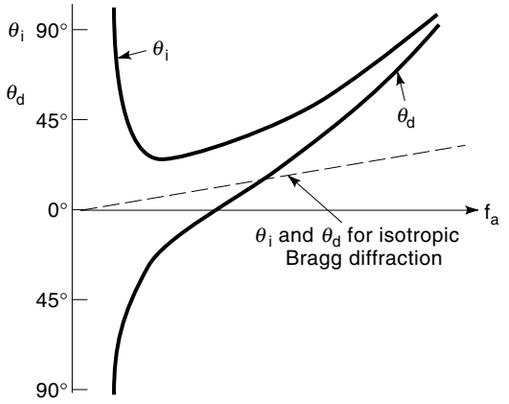

(b)

Figure 3. (a) Wave vector diagram for anisotropic acousto-optical Bragg diffraction in a plane orthogonal to the *C*-axis of a uniaxial crystal. (b) Variations of incident and diffraction angles versus acoustic frequency in anisotropic acousto-optical Bragg diffraction.

as well as the acoustic wave propagate in a plane orthogonal to the *C*-axis of a uniaxial crystal such as $LiNbO_3$. It has been established that conservation of both the frequency and the wave vector as expressed in Eqs. (1a, b) still holds. However, through optical anisotropy, both the refractive index and the polarization of the diffracted light differ from that of the incident or undiffracted light. It can be shown that the wave vector diagram depicted in Fig. 3(a) leads to the following expressions for the incident angle θ_i and the diffraction angle θ_d, which are both measured with respect to the acoustic wavefront:

$$\sin\theta_i = \frac{\lambda_0}{2n_i V_a}\left[f_a + \frac{V_a^2}{f_a\lambda_0^2}\left(n_i^2 - n_d^2\right)\right] \tag{2a}$$

$$\sin\theta_d = \frac{\lambda_0}{2n_i V_a}\left[f_a - \frac{V_a^2}{f_a\lambda_0^2}\left(n_i^2 - n_d^2\right)\right] \tag{2b}$$

where n_i and n_d designate the refractive indices of the incident and the diffracted light, respectively, and V_a and f_a are the velocity and frequency of the acoustic wave.

It is readily seen that the general expressions given in Eqs. (2a, b) reduce to the simple Bragg condition given by Eq. (1c) for an isotropic medium in which $n_d = n_i$. Figure 3(b) shows the plots for θ_i and θ_d as a function of the acoustic frequency. As a comparison, θ_i and θ_d $(= \theta_i)$ for isotropic Bragg diffraction are also plotted as a function of the acoustic frequency in Fig. 3(b).

From Fig. 3(a), we identify two special cases of practical importance. In the first case, the acoustic wave vector is tangential or near tangential to the locus of diffracted light wave vector, which is commonly called optimized anisotropic interaction; wave vector phase matching may be satisfied for a large range of acoustic frequency. As a result, large-bandwidth light beam deflectors and modulators may be constructed using this particular mode of interaction (26). For the second case in which the acoustic wave vector is collinear with both the incident and the diffracted light wave vectors, the collinear geometry involved facilities construction of electronically tunable AO filters for optical spectra (27).

The simultaneous availability of a variety of laser sources, piezoelectric transducer technology for efficient generation of very-high-frequency acoustic waves, and superior solid AO materials has enabled realization of various types of bulk AO devices including modulators, scanners, deflectors, Q-switches, mode lockers, tunable filters, spectrum analyzers, and correlators. Such bulk AO devices have now been deployed in a variety of commercial and military applications.

GUIDED-WAVE NONCOLLINEAR ACOUSTO-OPTIC INTERACTIONS

Basic Interaction Configuration and Mechanisms

A basic coplanar guided-wave AO interaction configuration is shown in Fig. 4 (12). The angle between the incident guided

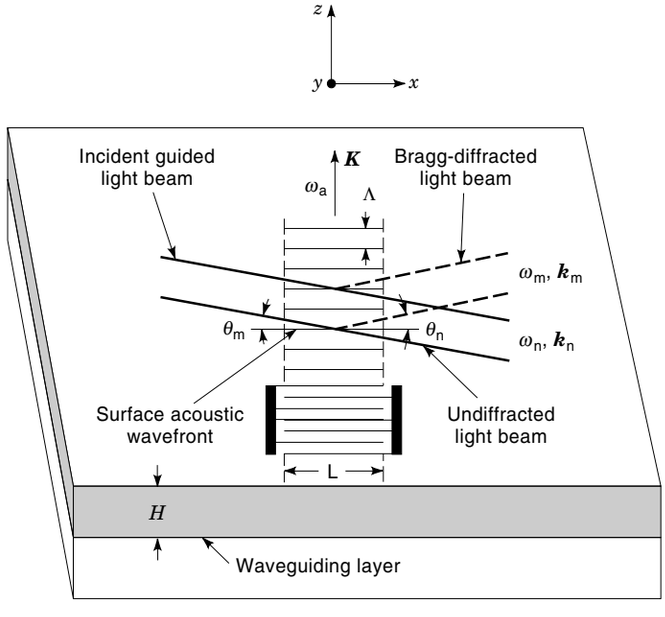

Figure 4. Guided-wave acousto-optical Bragg diffraction from a single-surface acoustic wave.

light and the SAW can vary from 90° (Raman–Nath regime), Bragg angle (Bragg regime) to 180° or 0° (collinear regime). In the case of Bragg regime, the basic elements corresponding to those in Fig. 2 for bulk-wave AO Bragg interaction are easily identified. The optical waveguide material should possess desirable acoustic, optical, and AO properties. The SAW is commonly excited by an interdigital electrode transducer (IDT) deposited upon the optical waveguide. If the substrate material is sufficiently piezoelectric, such as *Y*-cut $LiNbO_3$, the IDT may be deposited directly on it. Otherwise (e.g., GaAs or InP), a piezoelectric film such as ZnO (23,28,29) must be deposited either beneath or above the interdigital electrode array. The optical waveguide can be either a graded index layer created beneath the substrate or a step index layer deposited on top of the substrate. Examples of graded index guides are the $LiNbO_3$ waveguides formed by out- and in-diffusion techniques (30), whereas examples of step index guides are the glass (8) or As_2S_3 film (8) waveguides formed by sputtering or deposition. In either case, the waveguide layer is assumed to have an effective thickness or penetration depth *H*. Optical waveguide modes in such structures have been studied in detail (14–19).

As mentioned earlier, propagation of the SAW creates a moving optical grating in the optical waveguide. The SAW will also create moving corrugations at both the air-waveguide and waveguide–substrate interfaces. The moving grating and corrugations in turn cause diffraction of an incident guided light wave. Thus, except for the corrugations, the underlying mechanisms in coplanar guided-wave AO interactions are analogous to those in bulk-wave AO interactions. Even though the contribution resulting from the corrugations can be significant for certain ranges of waveguide thickness and acoustic wavelength, in most practical cases optical grating is the dominant mechanism in diffraction.

Similar to bulk-wave AO interaction, guided-wave AO diffraction may be either Ramon–Nath, Bragg, or collinear, depending upon the angle between the direction of the incident light and that of the SAW as well as the acoustic aperture. Ramon–Nath diffraction consists of a number of side orders when the AO parameter $Q \equiv 2\pi\lambda_0 L/n\Lambda^2$ is less than or equal to 0.3. The symbols λ_0 and Λ designate, respectively, the wavelengths of the guided optical wave (in free space) and the SAW; n is the effective refractive index of the guiding medium; and L designates the aperture of the SAW. When the light wave is incident at the Bragg angle defined earlier and Q is larger than 4π, diffraction is of the Bragg type and consists of only one side order. We shall limit our discussion to Bragg-type diffraction because this type of diffraction is capable of higher acoustic center frequency, wider modulation bandwidth, larger dynamic range, and thus greater versatility in application. Similarly, collinear AO diffraction is facilitated by having the SAW propagate in the same or opposite direction to that of the incident guided light wave.

It is important, however, to note that even though the basic interaction mechanisms for planar guided-wave acousto-optics is analogous to that of bulk-wave acousto-optics, the number of parameters involved in the guided-wave case is greater and the interrelation between them much more complex (11,12). For example, the diffraction efficiency is a sensitive function of the spatial distributions of both optical and acoustic waves, which in turn depends, respectively, on the guided optical modes and the optical and acoustic frequencies involved. In addition, in the case of a piezoelectric and electro-optical (EO) substrate such as $LiNbO_3$ and ZnO, the piezoelectric fields accompanying the SAW can be so large that the induced index changes because the EO effect becomes very significant (11).

Guided-Wave Noncollinear (Bragg) Acousto-Optic Interaction

General Treatment. The most common approach for treatment of AO interactions is the so-call couple-mode technique (8,10–12). This technique has been employed for the analysis of guided-wave AO Bragg diffraction from a single SAW in a $LiNbO_3$ planar waveguide (11). Such an analysis serves to reveal the physical parameters involved and the key device parameters as well as the performance limitations of the resulting devices. Both the analytical procedures and the methodology for numerical computation developed for this simple case can be conveniently extended to the case involving multiple SAWs (12) as well as other material substrates. Similar to bulk-wave AO Bragg diffraction, the relevant momentum (wave vector) and energy (frequency) conservation relations between the incident guided light wave, the diffracted guided light wave, and the SAW are expressed by Eq. (3a, b), where m and n designate the indices of the waveguide modes; $\boldsymbol{k}_n$, $\boldsymbol{k}_m$, and $\boldsymbol{K}$ are, respectively, the wave vectors of the diffracted light, the undiffracted light, and the SAW; and ω_n, ω_m, and ω_a are the corresponding radian frequencies:

$$\boldsymbol{k}_n = \boldsymbol{k}_m \pm \boldsymbol{K} \tag{3a}$$

$$\omega_n = \omega_m \pm \omega_a \tag{3b}$$

Figure 5(a) shows the wave vector diagram for the general case in which the diffracted light propagates in a waveguide mode (nth mode) that is different from the incident light (mth mode). The diffracted light may have a polarization parallel or orthogonal to that of the incident light. Again, as in bulk-wave AO Bragg diffraction, these two classes of interaction are called isotropic and anisotropic AO Bragg diffraction. As a special isotropic case, the diffracted light propagates in the same mode and thus has the same polarization as the incident light, as depicted in Fig. 5(b) ($n = m$). Many guided-wave AO Bragg diffraction experiments using $LiNbO_3$ and GaAs belong to this particular case (12). Figure 5(c) depicts a particularly interesting case of anisotropic diffraction in which the wave vector of the diffracted light is perpendicular or nearly perpendicular to that of the acoustic wave, commonly called optimized anisotropic diffraction (12). A specific example for the case in a *Y*-cut $LiNbO_3$ substrate, as depicted in Fig. 5(c), has been discussed (11,12).

The angles of incidence and diffraction measured with respect to the acoustic wavefront θ_m and θ_n are

$$\sin\theta_m = \frac{\lambda_0}{2n_m\Lambda}\left[1 + \frac{\Lambda^2}{\lambda_0^2}\left(n_m^2 - n_n^2\right)\right] \tag{4a}$$

$$\sin\theta_n = \frac{\lambda_0}{2n_n\Lambda}\left[1 - \frac{\Lambda^2}{\lambda_0^2}\left(n_m^2 - n_n^2\right)\right] \tag{4b}$$

where n_m and n_n are the effective refractive indices of the undiffracted and the diffracted light waves, and, as defined earlier λ_0 and Λ are the optical wavelength in free space and the wavelength of the SAW. Clearly, when the undiffracted, and

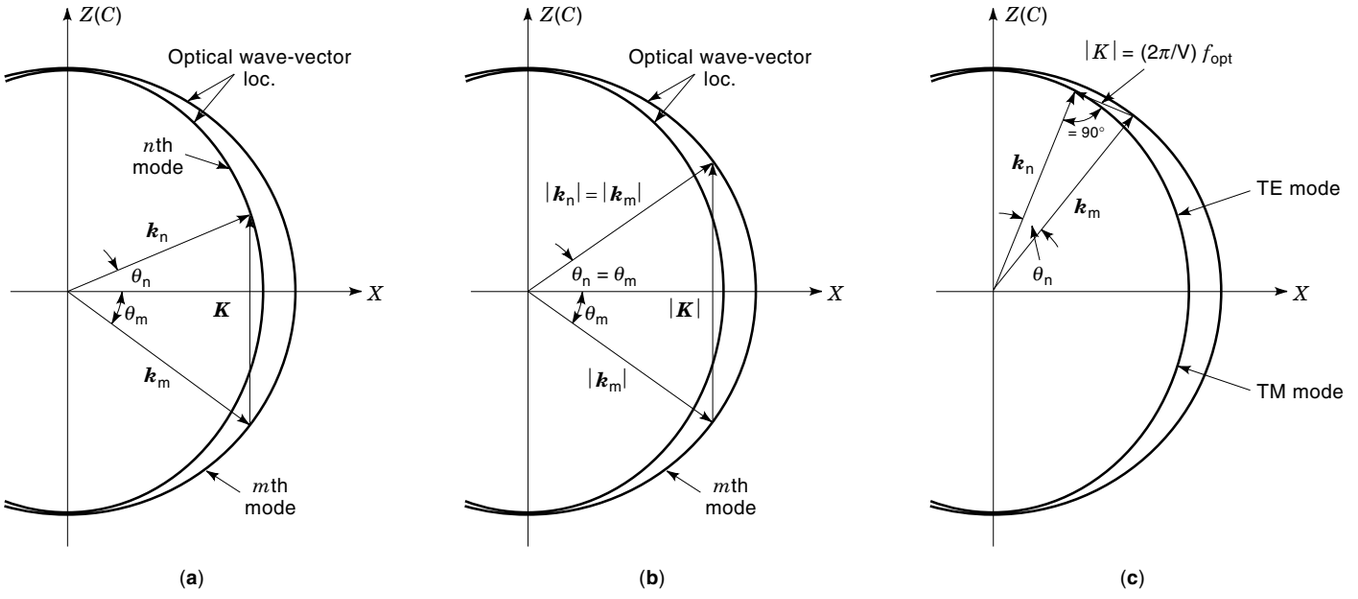

Figure 5. Phase-matching diagrams indicating wave vectors of incident light, Bragg-diffracted light, and surface acoustic wave in a *Y*-cut $LiNbO_3$ waveguide: (a) general case; (b) special isotropic case; (c) optimized anisotropic case.

diffracted light propagate in the same waveguide mode [Fig. 5(b)], we have $n_n = n_m$. For this particular case Eq. (4a, b) both reduce to the well-known Bragg condition in isotropic diffraction, namely, $\sin\theta_n = \sin\theta_m = (\lambda_0/2n_m\Lambda) = (\lambda_0\omega_m 4\pi n_m V_R)$, where $\theta_n = \theta_m$ is the so-called Bragg angle and V_R designates the propagation velocity of the SAW. Thus, the diffraction angle is identical to the incidence angle, and both angles increase linearly with the acoustic frequency because in practice the latter is much lower than the optical frequency.

Refer to the coordinate system of Fig. 4 and assume that the medium is lossless both optically and acoustically. First, appropriate forms for electric fields $E_m(x, y, z, t)$ and $E_n(x, y, z, t)$ of the undiffracted and diffracted light waves and the strain field $S(x, y, z, t)$ of the SAW and its accompanying piezoelectric field $E_p(x, y, z, t)$ are taken. Note again that the subscripts m and n designate, respectively, the waveguide modes of the undiffracted and diffracted light waves. Next, all the field quantities are substituted into the wave equation for the amplitude of the normalized electric fields of the optical waves $E_m(x)$ and $E_n(x)$ that depend on the x coordinate only as a result of interaction with the SAW. A set of coupled-wave equations for $E_m(x)$ and $E_n(x)$ is then obtained. Finally, these coupled-wave equations are solved subject to the boundary conditions $E_m(0) = 1$ and $E_n(0) = 0$ at the input $x = 0$, resulting in electrical fields of the undiffracted and the diffracted light waves at the output of the interaction region $x = L$ (11).

Diffraction Efficiency and Frequency Response of Basic Bragg Cell Modulator. From the electrical fields of optical waves referred to earlier, the diffraction efficiency $\zeta(f_a)$, defined as the ratio of diffracted light power at the output ($x = L$) and incident light power at the input ($x = 0$) of the interaction region, is found (11):

$$\zeta(f_a) = g^2(f_a)\left\{\frac{\sin\left[g^2(f_a) + (K\Delta\theta L/2)^2\right]^{1/2}}{\left[g^2(f_a) + (K\Delta\theta L/2)^2\right]^{1/2}}\right\}^2 \tag{5a}$$

where

$$g^2(f_a) \equiv \frac{\pi^2}{4\lambda_0^2}\frac{n_m^3 n_n^3 \left|\Gamma_{mn}(f_a)\right|^2 L^2}{\mathrm{Cos}\,\theta_m\,\mathrm{Cos}\,\theta_n} \tag{5b}$$

$$|\Gamma_{mn}(f_a)|^2 \equiv \frac{\left|\left[\int_{-\infty}^{\infty} U_m(y)U_n(y)\{p : SU_a(y) + r \cdot E_p U_p(y)\}\,dy\right]\right|^2}{\left|\left[\int_{-\infty}^{\infty} U_m^2(y)\,dy\right]\right|\left|\left[\int_{-\infty}^{\infty} U_n^2(y)\,dy\right]\right|} \tag{5c}$$

and

$f_a = \omega_a/2\pi$ = frequency of the SAW in cycle per second
$K = 2\pi/\Lambda$ = wave number of the SAW
L = aperture of the SAW
c = velocity of light in free space
$\Delta\theta$ = deviation of the incidence angle of the light from the Bragg angle

Also, $U_m(y)$, $U_n(y)$, $U_a(y)$, and $U_p(y)$ designate, respectively, the normalized field distributions (along the waveguide thickness) of the light waves, the acoustic wave, and the piezoelectric field. Finally, the following physical constants with suppressed vector and tensor subscripts are designated: p is the relevant photoelastic constant or constants, and r is the relevant electro-optic (EO) coefficient or coefficients. Thus, the terms $p : SU_a(y)$ and $r \cdot E_p U_p(y)$ are the contributions of the AO and EO effects, respectively.

The general expression given by Eq. (5a) can be used to calculate the diffraction efficiency and its frequency response as a function of both the polarization and the angle of incidence of the light (11). Equation (5a) reduces to the following simple form when the Bragg condition is satisfied ($\Delta\theta = 0$):

$$\zeta(f_a) = \sin^2 g(f_a) \tag{6}$$

It is seen that in contrast to bulk-wave AO Bragg interaction, the diffraction efficiency is a sensitive function of the spatial distributions of the diffracted and the undiffracted light waves as well as the frequency of the SAW as determined by the coupling function $|\Gamma_{mm}(f_a)|^2$. An efficient diffraction can occur only in the frequency range for which the confinement of the SAW matches that of the diffracted and undiffracted light waves. The dependence of the diffraction efficiency on acoustic, optical, and AO parameters is further complicated by the accompanying EO effect. Thus, in general, the coupling function $|\Gamma_{mm}(f_a)|^2$ is more complicated than the so-called overlap integral. Only for the special case in which the accompanying EO contribution is either negligible (e.g., in a glass waveguide) or proportional to the elasto-optical contribution will Eq. (5c) reduce to one that is simply related to the overlap integral.

For the same reason, it is impossible to define an AO figure of merit as simply as in a bulk-wave AO interaction. However, if we again consider the special case just mentioned and employ a simplified model, we may define the total power flow of the SAW P_a as

$$P_a = \frac{1}{2}\rho V_R^3 LS \int_{-\infty}^{\infty} U_a^2(y)\, dy \tag{7}$$

where ρ and V_R designate the density and the acoustic propagation velocity of the interaction medium, S designates the acoustic strain, and $\int_{-\infty}^{\infty} U_a^2(y)\, dy$ carries a dimension in length. Equations (5b, c) and (7) are now combined to give the following expression for $g^2(f_a)$:

$$g^2(f_a) = \left(\frac{\pi^2}{2\lambda_0^2}\right)\left(\frac{n_m^3 n_n^3 p^2}{\rho V_R^3}\right) C_{mn}^2(f_a)\left(\frac{L}{\cos\theta_m \cos\theta_n}\right) P_a \tag{8a}$$

where the frequency-dependent coupling coefficient $C_{mn}^2(f_a)$ is defined as

$$C_{mn}^2(f_a) \equiv \frac{\left[\int_0^{\infty} U_m(y) U_n(y) U_a(y)\, dy\right]}{\left[\int_{-\infty}^{\infty} U_m^2(y)\, dy\right]\left[\int_{-\infty}^{\infty} U_n^2(y)\, dy\right]\left[\int_{-\infty}^{\infty} U_a^2(y)\, dy\right]} \tag{8b}$$

Note that $C_{mn}^2(f_a)$ takes a form similar to the overlap integral, with its value depending upon the optical and the acoustic modes of propagation and equal to unity for bulk-wave AO interactions. Also, the factor $(n_m^3 n_n^3 p^2/\rho V_R^3)$ is similar to the bulk-wave AO figure of merit M_2 (6), henceforth designated by M_{2mn}.

From Eqs. (5a) and (8a, b) it is seen that for the case $g^2(f_a) \ll 1$ and $\Delta\theta \equiv 0$, the diffraction efficiency is approximately proportional to the total acoustic power P_a and is linearly proportional to the acoustic aperture.

We shall now examine the quantitative dependence of the diffraction efficiency on the acoustic frequency. From Eqs. (5a) and (8a) it is first noted that in contrast to the bulk-wave AO interaction, even at $\Delta\theta \equiv 0$, the diffraction efficiency is a sensitive function of the acoustic center frequency f_{a0} because of the frequency dependence of the SAW confinement. Thus, the bandwidth of a guided-wave AO Bragg modulator is mainly determined by the frequency dependence of three factors: the transducer conversion efficiency, the Bragg condition (phase matching), and SAW confinement. The individual and combined effects of these three factors on the frequency response can be determined using Eq. (5a, b) and a digital computer.

For the purpose of illustration, we now calculate the diffraction efficiency at the acoustic center frequency f_{a0} for the special case in which the EO contribution to the changes in refractive index is either negligible or proportional to the elasto-optical contribution. This calculation is applicable to special case involving nonpiezoelectric materials such as glass, oxidized silicon, and As_2S_3. We further assume that the power of the SAW is uniformly distributed in a depth of one acoustic wavelength (10). Thus as a special form of Eq. (7), we have

$$P_a = \frac{1}{2}\rho V_R^3 S^2 L\Lambda_0 = \frac{1}{2}\rho V_R^4 S^2\left(\frac{L}{f_{a0}}\right) \tag{9a}$$

or

$$S = \left(\frac{2P_a}{\rho V_R^4}\right)^{1/2}\left(\frac{f_{a0}}{L}\right)^{1/2} \tag{9b}$$

were Λ_0 designates the acoustic wavelength at the center frequency f_{a0}. Substituting Eq. (9b) into Eq. (5c) and combining Eqs. (5a, b) and (6) and restricting to the case of moderate diffraction, we obtain the following expression for the diffraction efficiency:

$$\zeta(f_{a0}) \approx g^2(f_{a0}) = \left(\frac{\pi^2}{2\lambda_0^2}\right) M_{2mn}\left(\frac{f_{a0}L}{V_R \cos\theta_m \cos\theta_n}\right) P_a \tag{10}$$

Equation (10) shows that, for this special case, the diffraction efficiency is proportional to the product of the center frequency and the aperture of the SAW as well as the total acoustic power.

We now turn to the AO Bragg bandwidth. In contrast to the bulk-wave interaction (3), the AO Bragg bandwidth in general cannot be expressed explicitly in terms of the center frequency and the aperture of the acoustic wave. Only for the special case in which $g^2(f_a) \ll (K\Delta\theta L/2)^2$ would Eq. (5a) lead to an expression similar to that of the bulk-wave case. For this special case, the absolute AO Bragg bandwidth for isotropic interaction with the TE_0 mode is given as follows:

$$\Delta f_{-3\text{dB.Bragg}} \approx \frac{1.8 n_0 V_R^2 \cos\theta_{B0}}{\lambda_0 f_{a0} L} \quad \text{(isotropic)} \tag{11a}$$

Or

$$\frac{\Delta f_{3\text{dB.Bragg}}}{f_{a0}} \approx \frac{1.8 n_0 V_R \cos\theta_{B0}}{\lambda_0 f_{a0}}\left(\frac{\Lambda_0}{L}\right) \quad \text{(isotropic)} \tag{11b}$$

where n_0 and θ_{B0} designate the effective refractive index and the Bragg angle for the TE_0 mode, and Λ_0 again designates

the wavelength of the SAW at the center frequency f_{a0}. The absolute AO Bragg bandwidth is inversely proportional to the product of the center frequency and the aperture of the SAW. Equation (11a, b) indicates clearly that the diffraction efficiency and the AO Bragg bandwidth impose conflicting requirements on the acoustic frequency and the acoustic aperture. In fact, the diffraction efficiency-Bragg bandwidth product is a constant that is independent of both the center frequency and the aperture of the SAW.

In summary, because of the complicated spatial distributions of the GOW and the SAW as well as the frequency dependence of the latter, numerical calculations using digital computers are required to determine the efficiency and exact frequency response of a guided-wave AO Bragg cell modulator. The procedure is as follows:

1. Obtain appropriate analytical expressions for the field distributions of the GOW and the SAW based on their directions and modes of propagation.
2. Include the frequency dependence of the amplitudes, phases, and penetration depth of the SAW.
3. Identify the relevant photoelastic and EO constants.
4. Calculate the diffraction efficiency versus the acoustic frequency using a digital computer, with the acoustic drive power as a parameter, and inserting the information derived in steps 1–3 together with the remaining optical and acoustic parameters into Eq. (5a).

Note that the frequency response of the SAW transducer can be incorporated in step 2.

Key Performance Parameters of Bragg Cell Modulator and Deflector. The planar guided-wave AO Bragg diffraction treated previously can be used to modulate and/or deflect a light beam. The resulting light beam modulators and deflectors, commonly called AO Bragg cell modulators, can operate at gigahertz acoustic center frequencies and over a wide RF band by using a variety of SAW transducer configurations; thus, they constitute useful devices for integrated and fiber-optical communication, computing, signal-processing, and sensing systems. The key device parameters that determine the ultimate performance characteristics of guided-wave AO modulators and deflectors are bandwidth, time–bandwidth product, acoustic and RF drive power, nonlinearity, and dynamic range. A brief discussion on each of these performance parameters now follows.

Bandwidth. As shown in the last subsection the diffraction efficiency-bandwidth product of a planar guided-wave AO modulator that employs isotropic Bragg diffraction and a single periodic interdigital (ID) SAW transducer (22) is rather limited. However, if the absolute modulator bandwidth is the sole concern, a large bandwidth can be realized by using either a single *periodic* ID SAW transducer with small acoustic aperture and small number of finger pairs or a single *aperiodic* ID SAW transducer with small acoustic aperture and large number of finger pairs (chirp transducers) (31,32). It should be emphasized, however, that in either case the large bandwidth is obtained at a reduced diffraction efficiency because of the very small interaction length. Consequently, a higher diffraction efficiency will necessarily require large RF or acoustic drive power. Therefore, it may be concluded that, for applications that require both wide bandwidth and high diffraction efficiency, more sophisticated SAW transducer configurations must be employed. It is now possible to realize high-performance planar guided-wave AO Bragg cell modulators with gigahertz center frequency and gigahertz bandwidth using these wide-band transducer configurations. The design, fabrication, testing, and measured performance figures for a variety of wide-band devices have been reported (11–13).

Time–Bandwidth Product. The time–bandwidth product of an AO modulator, TB, is defined as the product of the acoustic transit time across the incident light beam aperture and the modulator bandwidth (12). It is readily shown that this time–bandwidth product is identical to the number of resolvable spot diameters of an AO deflector, N_R, which is defined as the total angular scan of the diffracted light divided by the angular spread of the incident light. Thus the following well-known identities hold:

$$\mathrm{TB} = N_R = (D/V_R)\Delta f = \tau \Delta f \tag{12a}$$

$$\delta f_R = V_R/D \tag{12b}$$

$$\tau = D/V_R \tag{12c}$$

where D designates the aperture of the incident light beam, V_R is the velocity of the SAW, Δf is the device bandwidth, τ is the transit time of the SAW across the incident light beam aperture, and δf_R is the incremental frequency change required for deflection of one Rayleigh spot diameter. The acoustic transit time may be considered as the minimum AO switching time if the switching time of the RF driver is sufficiently smaller than the acoustic transit time. The desirable value for N_R depends upon the individual application. For example, in RF signal processing, it is desirable to have this value as large as possible because this value is identical to the processing gain. Thus, for this particular area of application, it is also desirable to have a collimated incident light beam of large aperture. Using a Y-cut $LiNbO_3$ optical waveguide, a guided-light beam aperture as large as 1.5 cm and good uniformity was demonstrated earlier at the author's laboratory. This light beam aperture resulted in an acoustic transit time of about 4.4 μs for a Z-propagation SAW (V_R = 3.488×10^5 cm/s). Because a deflector bandwidth of up to 1 GHz can be realized using multiple SAW transducers, so a time–bandwidth product as high as 4400 is achievable. At present, the acoustic attenuations measured in all other waveguide materials at 1 GHz are significantly higher, and thus considerably limit the maximum time–bandwidth product attainable.

In light modulation and single-port switching applications, on the other hand, it is desirable to have the time–bandwidth product as close to unity as possible so that the highest modulation or switching speed can be achieved. For this purpose, the incident light is focused to a small beam diameter at the interaction region so that the corresponding acoustic transit time is a minimum (33). Because it is possible to focus both the incident light to a spot size of a few micrometers using titanium in-diffusion proton-exchange (TIPE) waveguide lens in the Y-cut $LiNbO_3$ substrate (34) and the Z-propagating SAW in the same substrate using a curved transducer (35), a switching speed as high as 1 ns can be achieved.

Acoustic and RF Drive Power. Using Eqs. (7) and (9) and following the common practice of specifying the drive power

requirement for 50% diffraction, we simply set $\zeta(f_a)$ of Eq. (6) equal to 0.50 to arrive at the following expression for the required acoustic drive power at the center frequency f_{a0}:

$$P_a(50\%\ \text{diffraction}) = \left(\frac{\lambda_0^2 \cos\theta_m \cos\theta_n}{8}\right)\left(\frac{1}{M_{2mn.\text{eff}}}\right)\left(\frac{1}{L}\right) \tag{13a}$$

where

$$M_{2mn.\text{eff}} \equiv C_{mn}^2(f_{a0}) M_{2mn} \tag{13b}$$

Note that $C_{mn}^2(f_{a0})$ and M_{2mn} have been defined previously. To determine explicitly the total RF drive power P_e, we must first calculate the electrical-to-acoustic conversion efficiency T_c of the transducer used in the modulator or deflector. The frequency response and conversion efficiency of a periodic SAW IDT on $LiNbO_3$ substrates have been studied in detail in terms of one-dimensional equivalent circuits (22). Accordingly, the total RF drive power at 50% diffraction $P_e(f_{a0})$ is given by P_a (50% diffraction) divided by T_c. Clearly, both the total acoustic and RF drive powers required are inversely proportional to the acoustic aperture as in the bulk-wave modulator.

Finally, it is to be noted that, using some of the wide-band transducer configurations, the AO Bragg cell modulators requiring only milliwatts of electric drive power per megahertz of bandwidth at 50% diffraction efficiency with a bandwidth approaching 1 GHz can be realized.

Figure of Merit and Viable Substrate Materials

Based on the AO figure of merit M_{2mn} described in Eq. (8a) and the optical, acoustical, and AO properties of the existing materials, the following four viable materials have been identified. Among the many materials that have been explored experimentally for guided-wave AO devices, *Y*-cut $LiNbO_3$, nonpiezoelectrics such as oxidized Si, GaAs, and InP have demonstrated the highest potential. Relevant physical parameters of the four AO materials together with a few other potential AO materials are listed in Table 1. The excitation and propagation of GOWs and SAWs and the AO interactions involved have been studied most thoroughly for *Y*-cut $LiNbO_3$ (12) and GaAs, and to a lesser extent for nonpiezoelectric substrate materials. However, some significant experimental results have only been obtained recently for InP (36). A comparison of these substrate types now follows.

$LiNbO_3$ Substrate. As shown earlier, efficient and wide-band AO Bragg diffraction can be readily realized in a *Y*-cut $LiNbO_3$ substrate. Aside from a relatively high AO figure of merit, $LiNbO_3$ also possesses desirable acoustic and optical properties. As a result of large piezoelectricity, a SAW can be generated efficiently by directly depositing the IDT on the substrate. The typical propagation loss of the SAW is 1 dB/cm to 2 dB/cm at 1.0 GHz, which is by far the lowest among all AO materials that have been studied. Optical waveguides can be routinely fabricated using the well-established titanium in-diffusion (TI) technique (30). The measured optical propagation loss is typically 1.0 dB/cm, again the lowest among all existing AO materials. Furthermore, high-quality $LiNbO_3$ crystals of very large size are commercially available. Consequently, $LiNbO_3$ is at present the best substrate material for the realization of wide-band and efficient planar guided-wave AO Bragg cell modulators at gigahertz acoustic center frequencies.

SiO_2, As_2S_3, or SiO_2—Si Substrates. The second substrate type is composed of the nonpiezoelectric materials such as fused quartz (SiO_2), arsenic trisulfide (As_2S_3) (8), and oxidized silicon (SiO_2—Si) (29). Interest in these substrate materials is based on the fact that the first is a common optical waveguide material, the second is an amorphous material with a very large AO figure of merit, and the third may be used to capitalize on the existing silicon technology to further electrical and optical integrations. Even though it is common to deposit a piezoelectric zinc oxide (ZnO) film on such substrate materials for the purpose of SAW generation, ZnO—SiO_2 composite waveguides have also been used to facilitate guided-wave AO interaction because the ZnO film itself also possesses favorable optical waveguiding and AO properties. At the present time, measured propagation losses of the SAW in the ZnO—SiO_2—Si composite substrate (29,39) are much higher than those in the $LiNbO_3$ substrate and also considerably higher than those in the GaAs substrate. This contrast is accentuated as the acoustic frequency goes beyond 200 MHz. Thus, it may be concluded that until a composite substrate with a greatly reduced SAW propagation loss has been developed, guided-wave AO Bragg devices using the foregoing nonpiezoelectric substrate materials have to be limited to a consider-

Table 1. Relevant Physical Parameters of Acousto-Optic Materials

Material	Range of Optical Transmission (μm)	n_o	n_e	$n = (n_o + n_e)/2$	ρ (g/cm^3)	Acoustic Wave Polarization and Direction	V_s (10^5 cm/s)	Optical Wave Polarization and Direction	M_2 (10^{-18} s^3/g)	Photoelastic Coefficients
Fused quartz	0.2–4.5	—	—	1.46	2.2	Long.	6.95	$\perp$	1.51	$p_{11} = 0.121$, $p_{12} = 0.270$, $p_{44} = -0.075$
						Trans.	3.76	$\parallel$ or $\perp$	0.467	—
$LiNbO_3$	0.4–4.5	2.29	2.20	2.25	4.7	Long. in [11–20]	6.57	—	6.99	$p_{11} = 0.036$, $p_{12} = 0.072$, $p_{31} = 0.178$, $p_{13} = 0.092$, $p_{33} = 0.088$, $p_{41} = 0.155$
GaAs	1.0–11.0	—	—	3.37	5.34	Long. in [110]	5.15	$\parallel$	104	$p_{11} = -0.165$, $p_{12} = -0.140$, $p_{44} = 0.072$
						Trans. in [100]	3.32	$\parallel$ or $\perp$ in [010]	46.3	—
Gap	0.6–10.0	—	—	3.31	4.13	Long. in [110]	6.32	$\parallel$	44.6	$p_{11} = -0.151$, $p_{12} = -0.082$, $p_{44} = -0.074$

ably lower acoustic center frequency and a smaller bandwidth than those using the $LiNbO_3$ substrate.

GaAs Substrate. GaAs-band substrate can potentially provide the capability for the total or monolithic integration referred to previously because both the laser sources (40) and the photodetector arrays as well as the associated electronic devices may be integrated in the same GaAs substrate (41).

The AO Bragg cell modulators that have been realized use a Z-cut [001] GaAs waveguide substrate in which the SAW propagates in ⟨110⟩ direction (42a). A previous theoretical study (43) has predicted an AO Bragg bandwidth as large as 1.6 GHz and 1.4 GHz for the ⟨100⟩ and ⟨110⟩ propagation SAW, respectively, in a Z-cut GaAs—GaAlAs waveguide that supports a TE_0 mode at the optical wavelength of 1.15 μm.

The performance figures of the Bragg cell modulators at the optical wavelengths of 1.15 μm and 1.30 μm and at various RF frequency bands have been measured. Consider the one that used a tilted-finger chirp transducer centered at 485 MHz. A −3 dB AO bandwidth of 245 MHz and a diffraction efficiency of 5.0% at 1.0 W RF drive power were obtained. The highest acoustic center frequency that has been realized in the GaAs-based Bragg cell modulator was 1.1 GHz. The corresponding diffraction efficiency and AO bandwidth were 19.2% at 1.0 W RF drive power and 78 MHz (42b).

InP Substrate. As is true of the GaAs substrate, InP substrates can facilitate realization of monolithic integrated AO devices and circuits. Recently the prospects for ultimate realization of InP-based integrated AO devices has been greatly advanced in light of the continued successes in InP-based photonic integrated circuits (PICs) (44). Such PICs use the quaternary semiconductor material system of $In_{(1-x)}Ga_xAs_yP_{(1-y)}$ and the computer-controlled growth techniques of metal organic vapor-phase epitaxy (MOVPE) and molecular beam epitaxy (MBE) (45). By controlling the fractions (x, y) the band gap energy can be tailored in different regions of the InP material substrate, thus enabling monolithic integration of active components such as lasers and photodetectors and passive waveguide regions where AO and electro-optic (EO) interactions take place. Furthermore, by varying the fractions (x, y), the refractive index may be tailored to facilitate efficient optical interconnections between the active and passive components.

Figure 6 shows the configuration and geometry for guided-wave AO Bragg diffraction in the Z-cut {001} semi-insulating InP-based composite waveguide substrate that was studied recently (46).

The independent photoelastic constants of InP are known to be P_{11}, P_{12}, and P_{44} (40). The measured photoelastic constants of bulk InP crystals at 1.3 μm wavelength (47) are $P_{11} = -0.15$, $P_{12} = -0.13$, and $P_{44} = -0.05$. These values have suggested a large AO figure of merit, which is comparable to that of GaAs (42). For the AO interaction configuration shown in Fig. 6, the relevant strain components of the ⟨110⟩ (X)-propagation SAW are the $X(S_1)$ and $Z(S_3)$ components, and the photoelastic constants involved are P_{11} and P_{12}. The resulting induced changes of refractive indices responsible for Bragg diffraction are $(1/2)n_0^3(P_{11}S_1 + P_{12}S_3)$ and $(1/2)n_0^3(P_{12}S_1 + P_{11}S_3)$, respectively, for the light waves of TE- and TM-mode. Finally, the corresponding Bragg-diffracted light powers for the TE- and the TM-modes incident light are proportional to these induced index changes, respectively. Numerical calculations using the coupled-mode analysis (46) have shown that, at the acoustic center frequency around 200 MHz and the ZnO layer thickness of 0.25 μm, the overlap integral between the optical field and surface acoustic field distributions and, thus, the AO Bragg diffraction efficiency varies only slightly with the thickness of the InP cap layer. However, the Bragg diffraction efficiency decreases as the ZnO layer thickness and/or the SAW frequency increases.

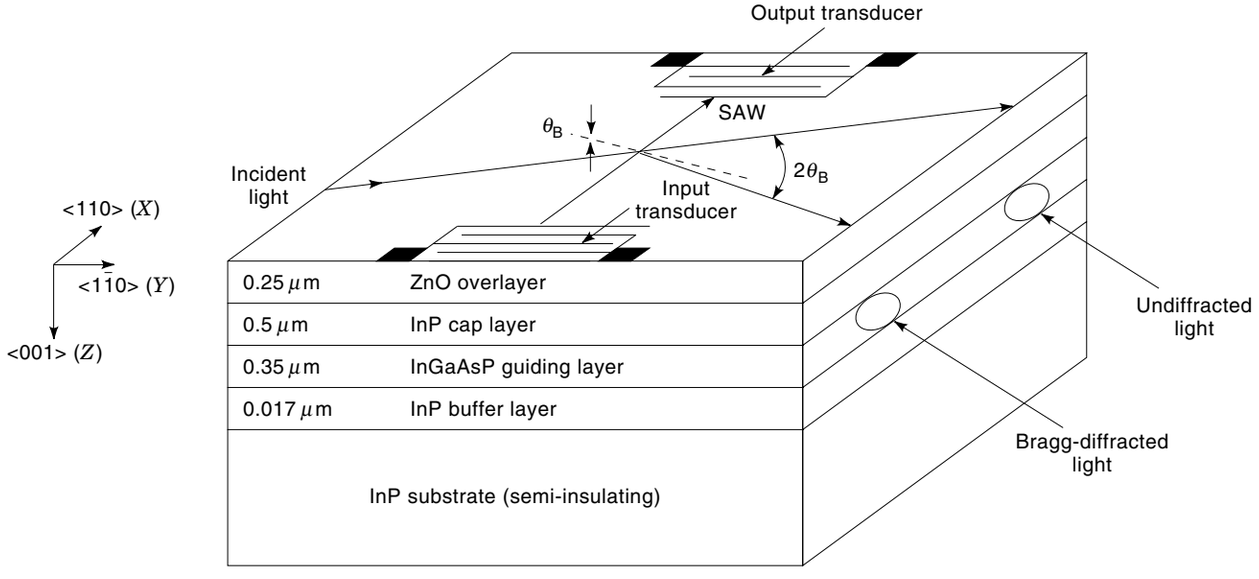

Figure 6. Configuration for guided-wave AO Bragg diffraction in InP/InGaAs/InP waveguide substrate.

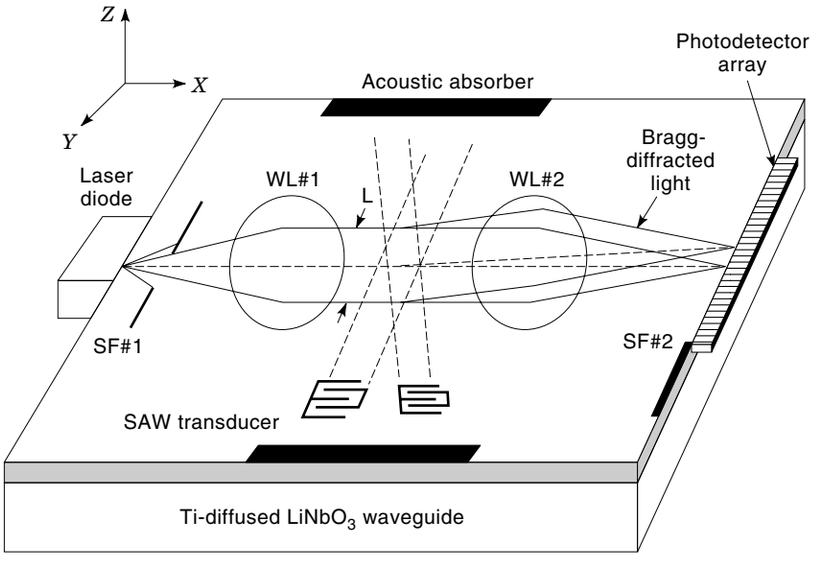

Figure 7. Integrated AO RF power spectrum analyzer module using hybrid integration in $LiNbO_3$ substrate. SF #1 and SF #2 are the spatial filters at the input and the output; WL #1 and WL #2 are the collimation and the focusing lenses.

For the measurement on AO Bragg diffraction, a semiconductor at 1.310 μm wavelength was used. The measured diffraction efficiencies for the TE_0- and TM_0-modes incident light at the acoustic center frequency of 167 MHz and an interaction length of 1.0 mm are 1.41% and 0.95%, respectively, at the acoustic drive power of 0.85 mW. The difference in the measured diffraction efficiency for the TE_0- and TM_0-modes incident light was in good agreement with the theoretical prediction. Based on the theoretical predictions and the experimental results reduction in the RF drive power by as much as two orders of magnitude can be achieved by incorporating changes in a new design of the transducer.

Fabrication Technologies. Construction of guided wave AO devices involves mainly fabrication of optical waveguide, SAW transducer, and waveguide lenses. For the $LiNbO_3$ substrate, both the titanium-indiffusion (TI) (30) and the proton-exchange (PE) (48) techniques, and their combination (TIPE) (49) have been refined to produce high-quality planar and channel waveguides. These techniques are readily employed to fabricate the planar and the channel waveguide arrays as well as their combinations in a common substrate required for construction of integrated AO device modules and circuits (13). As to formation of refractive waveguide lenses in the forms of collimation-focusing lens pairs and microlens arrays, the TIPE technique can also be conveniently employed (34). Recently, diffractive or grating waveguide lenses were formed in the $LiNbO_3$ waveguides using the ion-milling technique (50). Finally, formation of interdigital finger electrode transducers on the top of the $LiNbO_3$ waveguide for excitation of the SAW is routinely accomplished through the processing steps including preparation of photomask having the transducer IDT electrode pattern, deposition of metallic thin film, and replication of the IDT electrode pattern by using the lift-off technique (51).

For the GaAs and InAsP material systems, both the molecular beam epitaxy (45a), the metal organic chemical vapor deposition (MOCVD) (45b), and the MOVPE (44) have become the standard techniques for construction of high-quality planar and channel waveguides. Ion-milling using argon ions has also been developed to fabricate diffractive or grating waveguide lenses in GaAs material substrates (50a). Aspheric waveguide lenses have also been fabricated using selective chemical etching on the InP/InGaAsP material system (50b). With respect to efficient excitation of the SAW, it is necessary to first deposit a piezoelectric thin-film such as zinc oxide (ZnO) on the top of the waveguide and then fabricate the IDT electrode pattern upon it (42,43). Finally, the ZnO films are often grown using the RF sputtering technique.

Integrated AO Device Modules and Applications

$LiNbO_3$-Based Devices. An array of AO Bragg cell modulator-based integrated optic device modules with potential applications to information processing and communications (11–13) have been devised using the basic geometry of Fig. 4 and constructed using the substrate materials and fabrication technologies described earlier. The integrated AO device modules that have been realized include RF spectrum analyzers, light beam deflectors and scanners, optical frequency shifters, optical space switch arrays, optical correlators, and matrix multipliers. For example, one of the most active R and D efforts in the 1980s was focused upon the realization of the integrated optic RF spectrum analyzers (12). The basic architecture for such spectrum analyzers consists of a solid state laser source, a colimation-focusing waveguide lens pair, a wideband AO Bragg cell modulator, a waveguide photodetector array, and postprocessing electronic circuits. For the $LiNbO_3$ substrate, hybrid modules such as the one shown in Fig. 7 in which the diode laser source and the photodetector array are edge-coupled to the input and the output end faces of the $LiNbO_3$ substrate, respectively, have been realized (12).

However, the conventional AO Bragg cell-based RF power spectrum analyzers just described detect only the power and the frequency of the RF signals. Thus, not only the phase information of the RF signals is lost, but the dynamic range of detection is also severely limited. In order to alleviate all these disadvantages, an optical heterodyning detection scheme that incorporates a coherent optical reference beam must be used (13). Accordingly, it is desirable to implement the interferometric RF receivers, such as the spectrum analyzers, in planar integrated optic architecture format.

Figure 8(a) shows the architecture of a noncollinear interferometric RF spectrum analyzer module that was constructed in a *Y*-cut $LiNbO_3$ substrate, $1 \times 8 \times 16$ mm^3 in size (13). A tilted-finger chirp SAW transducer having a bandwidth of 205 MHz centered at 350 MHz was used to facilitate wideband AO Bragg diffraction, and thus produce the optical signal beam. An ion-milled grating concave lens was added to provide a divergent optical beam via passive Bragg diffraction of the undiffracted light, and thus the optical reference beam for heterodyning detection. Finally, a TIPE waveguide lens was placed at the output region of the substrate so that both focusing and Fourier transform functions were accomplished in the same waveguide substrate. Clearly, for an RF signal applied to the SAW transducer and thus a resulting optical signal beam, a corresponding optical reference beam that is coherent with and propagating in the same direction as the optical signal beam would be provided by the passive ion-milled grating. By design, these two Bragg-diffracted optical beams were made to match with each other and spread across the entire photodetector array, and then efficiently combined by the TIPE lens (34). Therefore, the optical alignment for the entire system is robust. The single-unit (basic) interferometric spectrum analyzer module just described has demonstrated the capability for simultaneously measuring the amplitude, frequency, and phase of RF signals using a 1 mW single mode He–Ne laser at the wavelength of 0.6328 μm (13). Encouraging performance figures including a bandwidth of 205 MHz centered at 350 MHz, a frequency resolution of 3.5 MHz, and single-tone simultaneous and two-tone third-order spurious-free dynamic ranges of 51 dB and 40 dB, respectively, were measured at the drive power of 50 mW per RF signal input. It should be noted that the measured 51 dB signal-tone dynamic range represents a 21 dB enhancement over that measured when the device module was operated as a conventional RF power spectrum analyzer.

Furthermore, a pair of the basic-unit interferometric devices just described were fabricated symmetrically in a *Y*-cut $LiNbO_3$ planar waveguide, also $1 \times 8 \times 16$ mm^3 in size, to form a dual-unit interferometric RF spectrum analyzer module, as shown in Fig. 8(b) (13). This dual-unit module was successfully used to determine the angle of arrival of RF signals in addition to their frequency, amplitude and phase, by measuring the phase differences between the heterodyned signals from the two identical units of the pair.

GaAs- and InP-Based Devices. As previously indicated, thus far, integrated optic RF spectrum analyzer modules of only the hybrid format were realized in the $LiNbO_3$ substrate because of our inability to integrate the lasers and photodetectors into the same substrate. In the mean time, GaAs and InP substrates provide the potential capability for total or monolithic integration because both the laser sources and the photodetectors as well as some associated optoelectronic devices can be fabricated in the same substrate of such compound semiconductor materials.

For the GaAs-based integrated optic RF power spectrum analyzers, a wideband AO Bragg cell modulator at GHz center frequency and a curved-contour hybrid waveguide lens pair in which the gratings lie in a *parabolic* contour, which is virtually coma-free up to $\pm 4°$ off-axis in a GaAs waveguide, have been realized (52). This curved-contour waveguide lens is capable of processing RF signals of GHz bandwidth. Finally, such hybrid waveguide lenses were integrated with a 50-element photodetector array of the InGaAs photoconducting type in the same GaAs waveguide 5×13 mm^2 in size as shown in Fig. 9 (52). The measured cross-talk between adjacent photodetector elements was lower than -14 dB as limited by the side-lobe level of the lens. The InGaAs photoconductive detector array has shown high gain (100 to 1000) at low frequency and a dynamic range of 35 dB, which suggests some potential for use in AO-based devices such as lightbeam switches/scanners in addition to the RF spectrum analyzers.

Recently, the prospects for realization of monolithic integrated AO signal processors has been greatly advanced through the continued successes in realization of InP-based PICs in the quaternary semiconductor material system of $In_{(1-x)}Ga_xAs_yP_{(1-y)}$ (44).

The first construction of guided-wave AO Bragg cell modulator in a composite InP/InGaAsP/InP planar waveguide was reported most recently (46). Figure 6 shows the configuration

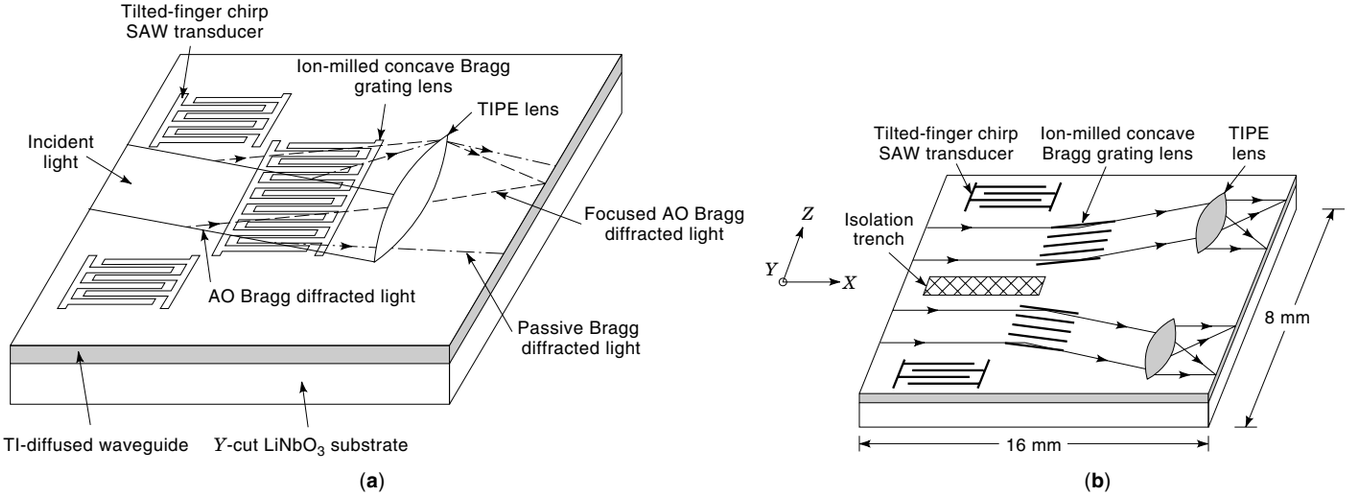

Figure 8. Integrated AO interferometric RF spectrum analyzer module in $LiNbO_3$ substrate (a) a basic unit and (b) a dual unit.

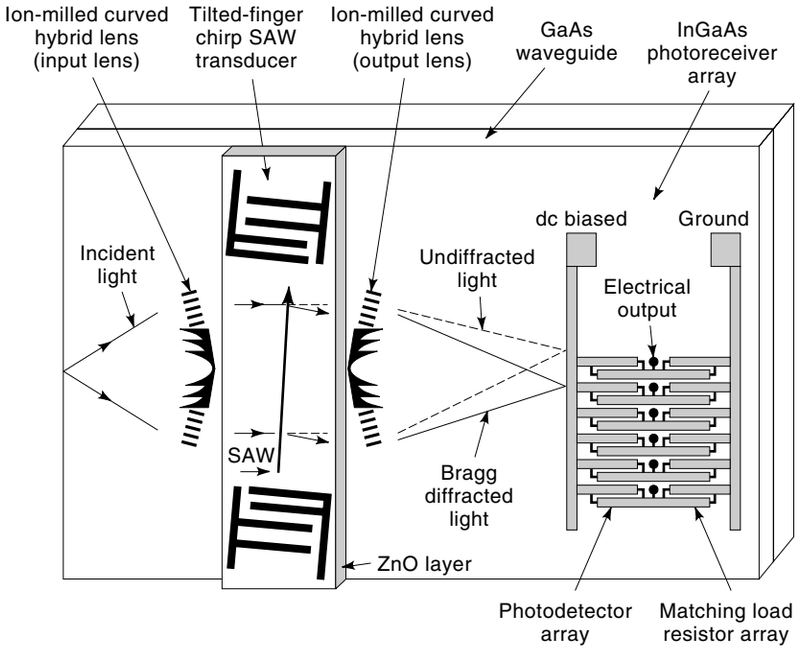

Figure 9. An integrated AO RF power spectrum analyzer module in GaAs substrate.

and geometry in the *Z*-cut {001} semi-insulating InP-based composite waveguide substrate used. The waveguide sample was prepared by the MOVPE method and composed of three layers: 0.017 μm InP buffer layer, 0.35 μm $In_{0.22}Ga_{0.78}As_{0.47}P_{0.53}$ guiding layer, and 0.5 μm InP cap layer. A 0.25 μm piezoelectric film of ZnO was subsequently deposited, using the RF sputtering technique, on the top of the InP/InGaAsP/InP composite waveguide. The ZnO film served to enhance the transduction efficiency for the SAW that propagates in the $\langle 110 \rangle$ direction. The finished waveguide sample was then cleaved along the $\langle 110 \rangle$ direction to facilitate the input and output coupling of the light beams. Finally, the sample was also cleaved along the $\langle 1\bar{1}0 \rangle$ direction into the size of 4×6 mm^2. The measured diffraction efficiencies for the TE_0- and TM_0-modes incident light at 1.310 μm and the acoustic center frequency of 167 MHz and interaction length of 1.0 mm are 1.41% and 0.95%, respectively, at the acoustic drive power of 0.85 mW. We note that, when the incident light was propagated in the TE_0-mode, a diffraction efficiency as high as 14% was measured at an acoustic drive power of 8.5 mW. Based on the theoretical predictions and the experimental results obtained, improvement in terms of diffraction efficiency per millimeter interaction length per watt RF drive power by as much as two orders of magnitude can be achieved by incorporating changes in design of the SAW transducer.

Table 2. Demonstrated Applications of Guided-Wave Acousto-Optic Bragg Cell Modulators

I.	Radio-Frequency Signal Processing
	Spectral analysis or Fourier transform
	Pulse compression
	Convolution
	Time- and space-integrating correlations
	Adaptive filtering
	Ambiguity function
	Programmable analog and digital correlation and filtering
II.	Communications
	Light-beam modulation and deflection
	Multiport switching
	Space-, time-, and wavelength-division multiplexing/demultiplexing
	Tunable optical wavelength filtering
	Optical-frequency shifting and heterodyne detection
	Optical interconnect

Applications of Integrated AO Bragg Cell Device Modules. It is clear that all of the potential applications listed in Table 2 can be implemented using the additional integrated AO device modules presented in the last subsections. Even though significantly improved performance figures can be expected in some of these device modules, significantly higher degree of miniaturization and integration can also be realized in others. As with the bulk-wave AO devices, all such integrated AO device modules do not involve any mechanical moving parts.

GUIDED-WAVE COLLINEAR ACOUSTO-OPTIC INTERACTIONS

General Treatment-Guided-Mode to Guided-Mode Conversion with Polarization Rotation

Bulk optical tunable filters using collinear and noncollinear AO interactions have been explored with fruitful results since the late 1960s (53,54). Subsequently, their guided-wave counterparts have been explored (55–69).

Figure 10 shows the interaction configuration involving guided-mode to guided-mode conversion with polarization rotation in T/I–$LiNbO_3$ planar waveguide. The optical waveguide supports both the TE_0- and TM_0-guided modes. An interdigital SAW transducer is fabricated on top of the optical waveguide to generate the SAW. Both the incident guided-

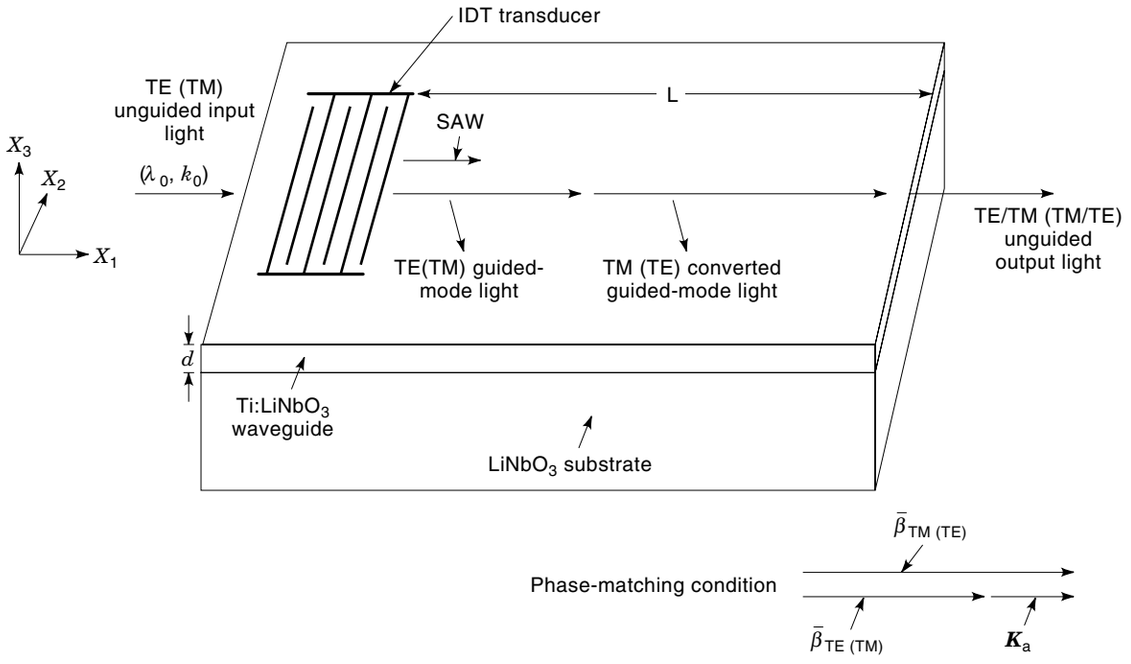

Figure 10. Geometry for guided-wave collinear acousto-optic mode conversion in Ti–LiNbO$_3$ waveguides.

mode light, in either the TE_0 or TM_0 polarization, and the SAW propagate in the positive X_1 direction. The mode conversion from the incident TE_0 guided-mode light into the TM_0 guided-mode light, or vice versa, induced by a copropagating SAW as shown in Fig. 10, is analyzed using the coupled-mode theory (55,56).

The coupling between the incident guided-mode light and the SAW results in a wavelength-converted light with orthogonal polarization when one of the following phase-matching conditions is satisfied:

$$\overline{\beta}_{TE} - \overline{\beta}_{TM} + \overline{K}_a = 0 \,(\text{for the TE}_0 \rightarrow \text{TM}_0 \text{ mode conversion}) \tag{14a}$$

and

$$\overline{\beta}_{TM} - \overline{\beta}_{TE} + \overline{K}_a = 0 \,(\text{for the TM}_0 \rightarrow \text{TE}_0 \text{ mode conversion}) \tag{14b}$$

In Eq. (14a, b), $\overline{\beta}_{\text{TE}}$ and $\overline{\beta}_{\text{TM}}$ denote the propagation constants of the TE_0 and TM_0 guided-mode light, respectively, and $\mathbf{K}_a$ the propagation constant of the SAW.

The coupled-wave equations describing the TE⇔TM mode conversion can be written in the following differential form (62):

$$\frac{dE_{\text{TE}}(x_1)}{dx_1} = -j\kappa E_{\text{TM}}(x_1)e^{-j2\Delta\beta x_1} \tag{15a}$$

$$\frac{dE_{\text{TE}}(x_1)}{dx_1} = -j\kappa E_{\text{TM}}(x_1)e^{+j2\Delta\beta x_1} \tag{15b}$$

where E_{TE} and E_{TM} designate, respectively, the normalized complex amplitudes of the TE- and TM-optical waveguide modes involved, $2\Delta\beta$ and κ the phase mismatch and the overlap integral between the optical guided-modes (or the coupling coefficient) and the SAW field distributions defined as follows:

$$2\Delta\beta = \left|\boldsymbol{\beta}_{\text{TE}} - \boldsymbol{\beta}_{\text{TM}} - \boldsymbol{K}_a\right| \,(\text{for the TE}_0 \rightarrow \text{TM}_0 \text{ mode conversion}) \tag{16a}$$

and

$$2\Delta\beta = \left|\boldsymbol{\beta}_{\text{TM}} - \boldsymbol{\beta}_{\text{TE}} - \boldsymbol{K}_a\right| \,(\text{for the TM}_0 \rightarrow \text{TE}_0 \text{ mode conversion}) \tag{16b}$$

$$\kappa = \frac{\omega\epsilon_0}{4}\int_{-\infty}^{\infty} \overline{E}^*_{\text{TM}}[\Delta\epsilon]\overline{E}_{\text{TE}}\,dx_3 \quad (\text{for TE}_0 \rightarrow \text{TM}_0 \text{ mode conversion}) \tag{16c}$$

and

$$\kappa = \frac{\omega\epsilon_0}{4}\int_{-\infty}^{\infty} \overline{E}^*_{\text{TE}}[\Delta\epsilon]\overline{E}_{\text{TM}}\,dx_3 \quad (\text{for TM}_0 \rightarrow \text{TE}_0 \text{ mode conversion}) \tag{16d}$$

where $[\Delta\epsilon]$, a function of κ_3, denotes the strain-induced changes in permittivity tensor $[\epsilon]$ (70), calculated at unit acoustic drive power density, given by Eq. (16e) in which $[\Delta B]$ denotes the induced changes in impermeability tensor.

$$[\Delta\epsilon] \cong -[\epsilon][\Delta B][\epsilon] = 1/2[\Delta\epsilon(\chi_3)]\exp(jK_a\chi_1) + \text{Complex Conjugate} \tag{16e}$$

Note that $[\Delta B]$ depends on the photoelastic coefficients (p_{ij}) and electro-optic coefficients (r_{ij}) (40) of the $LiNbO_3$ substrate relevant to the crystal-cut and SAW propagation direction involved. For the configuration of Z-cut X-propagation

SAW the specific coefficients involved are p_{11}, p_{22}, p_{41}, p_{44}, and r_{22}. For the configuration of X-cut Y-propagation SAW, the specific coefficients are p_{41}, p_{44}, and r_{22}. The numerical values for these relevant photoelastic and electro-optic coefficients are taken from Ref. 71. Again, in Eqs. (16c) and (16d) $\boldsymbol{E}_{\mathrm{TE}}$ and $\boldsymbol{E}_{\mathrm{TM}}$ are the electric field vectors of the TE_0- and TM_0-modes of the light, respectively, calculated under power normalization.

For the uniform grating of Fig. 10, the coupling coefficient κ is uniform throughout the interaction length and is expressed as follows (61,62):

$$\kappa^2 = \frac{\pi^2}{2\lambda^2} M I_{\mathrm{a}} \Gamma^2 \tag{17}$$

where λ is the optical wavelength of operation, I_{a} is the acoustic intensity of the SAW along the cross-section of the optical waveguide, Γ is the overlap integral of the optical field distributions of the TE and TM modes and the acoustic field distribution of the SAW, and M is the AO figure of merit given by

$$M \equiv \frac{(n_{\mathrm{TE}} n_{\mathrm{TM}})^3 p^2}{\rho V_{\mathrm{R}}^3} \tag{18}$$

in which n_{TE} and n_{TM} are the effective refractive indices of the TE and TM modes, ρ is the density of the material, p is the relevant photoelastic tensor component (p_{41} for X–Y and Y–X $LiNbO_3$ substrates), and V_{R} is the velocity of the SAW.

Key Performance Parameters of Guided-Wave AO Tunable Filter

A summary of the major performance characteristics of the resulting integrated acousto-optic tunable filters (AOTF) now follows.

Acoustic Center Frequency. From Eq. (14), the relation between the acoustic center frequency f_{a} and the selected (filtered) optical center wavelgnth λ_0 is derived as follows:

$$f_{\mathrm{a}} = V_{\mathrm{a}} \Delta n_{\mathrm{eff}} / \lambda_0 \tag{19a}$$

where V_{a} is the velocity of the SAW at the acoustic frequency f_{a} in the Ti–$LiNbO_3$/$LiNbO_3$ substrate, and the birefringence Δn_{eff} is defined as follows:

$$\Delta n_{\mathrm{eff}} \equiv \left| n_{\mathrm{eff}}^{\mathrm{TM}} - n_{\mathrm{eff}}^{\mathrm{TE}} \right| = \left| \overline{\beta}_{\mathrm{TM}} - \overline{\beta}_{\mathrm{TE}} \right| / k_0 \tag{19b}$$

in which $n_{\mathrm{eff}}^{\mathrm{TE}}$ and $n_{\mathrm{eff}}^{\mathrm{TM}}$ are the effective refractive indices of the TE_0 and TM_0 guided-mode light, respectively, and k_0 is the propagation constant of the incident light in free-space.

Mode Conversion Efficiency. The $\mathrm{TE}_0 \rightarrow \mathrm{TM}_0$ (or $\mathrm{TM}_0 \rightarrow \mathrm{TE}_0$) mode-conversion eficiency η is derived as follows using the coupled-mode analysis (62).

$$\eta = \sin^2 \left\{ \left(\sqrt{|\kappa|^2 P_{\mathrm{a}} + (\Delta\beta)^2} \right) L \right\} \Big/ \{1 + (\Delta\beta)^2 / (P_{\mathrm{a}} |\kappa|^2)\} \tag{20}$$

where L and P_{a} denote the interaction length and the acoustic drive power density, respectively, and the phase mismatch parameter $2\Delta\beta$ and the coupling coefficient κ have been defined previously.

Acoustic Drive Power Density Requirement. Using Eq. (20), and under the condition of perfect phase matching ($\Delta\beta = 0$), the acoustic drive power density required for 100% mode conversion, P_{100}, is derived as follows:

$$P_{100} = \{\pi / (2|\kappa|L)\}^2 \tag{21}$$

The corresponding RF drive power requirement is readily determined by the conversion efficiency of the SAW transducer.

Optical Bandwidth. The optical bandwidth associated with the collinear AO mode conversion in the $LiNbO_3$ substrate at the optical center wavelength of interest is typically very narrow (<10 nm). Consequently, the birefringence Δn_{eff}, as given in Eq. (19b), may be considered independent of the optical wavelength within the range defined by the optical bandwidth at the center wavelength λ_0. Accordingly, at a fixed acoustic frequency f_{a}, the wavelength deviation $\delta\lambda$ from the perfect phase matching condition can be written as

$$2\Delta = \Delta n_{\mathrm{eff}} \frac{2\pi}{\lambda} - |\boldsymbol{K}_{\mathrm{a}}| = \Delta n_{\mathrm{eff}} \frac{2\pi}{\lambda} - \Delta n_{\mathrm{eff}} \frac{2\pi}{\lambda_0} \approx \Delta n_{\mathrm{eff}} \frac{2\pi}{\lambda_0^2} \delta\lambda \tag{22}$$

where $\lambda \equiv \lambda_0 \pm \delta\lambda$.

Using Eq. (22), the mode-conversion efficiency in Eq. (20) can be rewritten as follows:

$$\eta = \left[\sin^2 \left(\chi |\kappa| \sqrt{P_{\mathrm{a}}} L \right) \right] / \chi^2 \tag{23}$$

where

$$\chi = \sqrt{1 + \left(\pi \Delta n_{\mathrm{eff}} \delta\lambda \Big/ \lambda_0^2 |\kappa| \sqrt{P_{\mathrm{a}}} \right)^2} \tag{24}$$

When the acoustic drive power density P_{a} in Eq. (23) is set equal to P_{100} and the mode conversion efficiency η in Eq. (23) set equal to 0.5% or 50%, the following expression for $2\delta\lambda$ (full-width at half-maximum, FWHM) is obtained:

$$\mathrm{FWHM} = 2\delta\lambda = 2 \times 0.4 \lambda_0^2 / L \Delta n_{\mathrm{eff}} \tag{25a}$$

or

$$\delta\lambda / \lambda_0 = 0.4 (\Lambda_0 / L) \tag{25b}$$

where $\Lambda_0 = V_{\mathrm{a}} / f_{\mathrm{a}}$ is the center wavelength of the SAW. Equations (25a, b) state that at given optical and acoustic center wavelengths the optical bandwidth is inversely proportional to the interaction length.

Table 3. Refractive Indices of the $LiNbO_3$ Substrate

Optical Wavelength, λ (μm)	Refraction Indices of the $LiNbO_3$ Substrate	
	Ordinary	Extraordinary
0.50	2.34272	2.24785
0.80	2.25723	2.17526
1.15	2.22918	2.15123
1.31	2.22180	2.14493
1.55	2.21283	2.13730

Table 4. Calculated Effective Refractive Indices of the Ti:$LiNbO_3$ Waveguide

Optical Wavelength, λ (μm)	Waveguide Thickness, d(μm)	*X*-Cut Configuration		*Z*-Cut Configuration	
		TE	TM	TE	TM
0.50	0.6	2.26312	2.34708	2.34795	2.26797
		2.27885	2.35464	2.35503	2.27881
	1.0	2.25404			2.25400
		2.28327	2.35846	2.35861	2.28334
	1.5	2.26981	2.34674	2.34723	2.27008
		2.24614			
0.80	1.0	2.19673	2.26203	2.26864	2.19596
		2.20505	2.26817	2.27045	2.20487
	1.5	2.17796			2.17764
		2.20886	2.27139	2.27165	2.20884
	2.0	2.19035	2.25727	2.25756	2.19033
1.15	1.2	2.16769	2.23113	2.23202	2.16644
	1.5	2.17363	2.23457	2.23540	2.17290
	2.0	2.17968	2.23901	2.23956	2.17938
1.31	1.2	2.15751	2.22228	2.22296	2.15593
	2.0	2.17084	2.22968	2.23036	2.17037
	2.5	2.17490	2.23286	2.23333	2.17469
		2.148105			2.14822
1.55	1.5	2.15489	2.21381	2.21461	2.15001
	2.0	2.15937	2.21798	2.21883	2.15858
	2.5	2.16429	2.22151	2.22214	2.16345

Table 5. Filter Performance Figures at the Interaction Length of 30 mm

λ (μm)	d (μm)	*X*-Cut Configuration				*Z*-Cut Configuration			
		f_a (MHz)	P_{100} (mW/mm)	FWHM (nm)	$\Delta\lambda_{3dB}$ (nm)	f_a (MHz)	P_{100} (mW/mm)	FWHM (nm)	$\Delta\lambda_{3dB}$ (nm)
0.50	0.6	587.7	1.74	0.79	120	607.4	0.17	0.78	114
	1.0	567.9	0.95	0.83	113	578.8	0.28	0.82	113
	1.5	563.4	0.49	0.84	112	571.6	0.80	0.83	111
0.80	1.0	305.8	15.5	2.51	376	317.7	0.82	2.43	430
	1.5	295.6	11.3	2.59	320	302.7	1.10	2.59	541
	2.0	292.8	6.80	2.61	314	298.1	1.60	2.66	516
1.15	1.2	206.7	70.2	5.27	279	216.5	2.60	5.25	620
	1.5	198.5	65.0	5.60	514	206.4	2.72	5.53	766
	2.0	193.3	47.2	5.80	438	198.7	3.08	5.74	910
1.31	1.2	186.3	130.6	6.96	435	195.5	5.45	6.96	524
	2.0	169.6	80.2	7.64	510	175.2	5.10	7.50	1009
	2.5	167.2	50.8	7.76	485	171.3	6.30	7.67	1127
1.55	1.5	142.4	245.1	10.52	578	158.3	7.45	10.11	719
	2.0	141.7	235.0	11.25	666	147.6	6.62	10.90	1156
	2.5	138.3	185.5	11.50	578	142.8	7.6	11.30	1300

Table 6. Filter Performance Figures at Guiding Layer Thickness for (a) Minimum Acoustic Drive Power Density for 100% $TE_0 \rightarrow TM_0$ or $TM_0 \rightarrow TE_0$ Mode Conversion and (b) Largest Optical Wavelength Tuning Range at 100% Mode Conversion and Transducer Bandwidth of 200 MHz

		Minimum Acoustic Drive Power Density					Largest Optical Wavelength Tuning Range				
	λ (μm)	d (μm)	f_a (MHz)	P_{100} (mW/mm)	FWHM (nm)	$\Delta\lambda_{3dB}$ (nm)	d (μm)	f_a (MHz)	P_{100} (mW/mm)	FWHM (nm)	$\Delta\lambda_{3dB}$ (nm)
X-cut	0.50	1.5	563.4	0.49	0.84	112	0.6	587.7	1.74	0.79	120
	0.80	2.0	292.8	6.80	2.61	314	1.0	305.8	15.5	2.51	376
	1.15	2.0	193.3	47.2	5.80	438	1.5	198.5	65.0	5.60	514
	1.31	2.5	167.2	50.8	7.76	485	2.0	169.6	80.2	7.64	510
	1.55	2.5	138.3	185.5	11.50	578	2.0	141.7	235.0	11.25	666
Z-cut	0.50	0.6	607.4	0.17	0.78	114	0.6	100	0.17	0.78	114
	0.80	1.0	317.7	0.82	2.43	430	1.5	302.7	1.10	2.59	541
	1.15	1.2	216.5	2.60	5.25	620	2.0	198.7	3.08	5.74	910
	1.31	2.0	175.2	5.10	7.50	1009	2.5	171.3	6.30	7.67	1127
	1.55	2.0	147.6	6.62	10.90	1156	2.5	142.7	7.6	11.30	1300

Optical Wavelength Tuning Range. The tuning range for filtered optical wavelength is determined by the bandwidth of the SAW transducer and the dependence of the overlap integral [Eqs. (16c, d)] on the optical and acoustic wavelengths. In the former, the reduced acoustic drive power density at acoustic frequencies outside of the transducer bandwidth will result in a decrease in the mode-conversion efficiency at the filtered optical wavelength, even though the perfect phase matching condition is fulfilled. In the latter, the dependence of the overlap integral on the optical and acoustic wavelengths or frequencies will result in a corresponding decrease in the mode-conversion efficiency, even though the acoustic drive power density remains the same.

For simplicity, we first assume that the transducer bandwidth (Δf_a) is sufficiently large so that the mode-conversion efficiency is solely determined by the dependence of the overlap integral on the optical wavelength and the acoustic frequency. Accordingly, the tuning range for filtered optical wavelength $\Delta\lambda_{3dB}$ centered at λ_0 is determined by the upper and lower wavelengths $\lambda_{3dB,H}$ and $\lambda_{3dB,L}$, at which the mode-conversion efficiency is reduced to half that at its peak; in other words,

$$\Delta\lambda_{3dB} = \lambda_{3dB,H} - \lambda_{3dB,L} \tag{26}$$

Although it is rather tedious to present the explicit expressions for $\lambda_{3dB,H}$ and $\lambda_{3dB,L}$, they may readily be calculated numerically using Eqs. (16) and (17).

Similarly, the effect of transducer bandwidth on the optical wavelength tuning range can be readily calculated as the optical center wavelength, the acoustic center frequency, and the transducer bandwidth are specified.

Filter Performance Characteristics at Practical Optical Center Wavelengths

It has been shown that for a SAW copropagating with the guided-light wave, the phase-matching conditions corresponding to the $TE_0 \rightarrow TM_0$ (see Eq. 14a) and to the $TM_0 \rightarrow TE_0$ (see Eq. 14b) mode conversions can be fulfilled only in the *X*-cut and *Z*-cut Ti–$LiNbO_3$ waveguides, respectively. The analytical expressions presented earlier in this section have been used to evaluate the performance characteristics and figures of the integrated AOTF in the *X*- and *Z*-cut Ti–$LiNbO_3$/$LiNbO_3$ waveguides of step-index profile, with the SAW propagating in the *Y*- and *X*-direction, respectively. The numerical calculations have been carried out for the five practical optical center wavelengths, namely, $\lambda_0 = 0.50\ \mu$m, $0.80\ \mu$m, $1.15\ \mu$m, $1.31\ \mu$m, and $1.55\ \mu$m, and the results presented in plots. The corresponding ordinary and extraordinary refractive indices of the $LiNbO_3$ substrate used are compiled in Table 3. The increases in the ordinary (Δn_o) and extraordinary (Δn_e) refractive indices due to the Ti-indiffusion process are set equal to the established values of 0.02 and 0.04, respectively. For each optical center wavelength, three guiding layer thicknesses are considered, namely, $d = 0.6\ \mu$m, $1.0\ \mu$m, and $1.5\ \mu$m at $\lambda_0 = 0.5\ \mu$m; $d = 1.0\ \mu$m, $1.5\ \mu$m, and $2.0\ \mu$m at $\lambda_0 = 0.8\ \mu$m; $d = 1.2\ \mu$m, $1.5\ \mu$m, and $2.0\ \mu$m at $\lambda_0 = 1.15\ \mu$m, $d = 1.2\ \mu$m, $2.0\ \mu$m, and $2.5\ \mu$m at $\lambda_0 = 1.31\ \mu$m, and $d = 1.5\ \mu$m, $2.0\ \mu$m, and $2.5\ \mu$m at $\lambda_0 = 1.55\ \mu$m. The resulting guided-modes and their effective refractive indices are given in Table 4. Note that the guiding layer thicknesses of $0.6\ \mu$m, $1.0\ \mu$m, $1.2\ \mu$m, $1.2\ \mu$m, and $1.5\ \mu$m are very close to the cut-off values for the fundamental mode (TE_0 or TM_0) at the optical wavelengths of $0.5\ \mu$m, $0.8\ \mu$m, $1.15\ \mu$m, $1.31\ \mu$m, and $1.55\ \mu$m, respectively. The calculated performance figures are summarized in Tables 5 and 6.

The performance figures summarized in Tables 5 and 6 should serve as a useful guideline for design and construction of the IAOTFs. For example, at the optical center wavelength of the blue-green region (e.g., $0.50\ \mu$m), performance figures of the AOTFs including an acoustic drive power requirement as low as 0.17 mW/mm for 100% $TM_0 \rightarrow TE_0$ mode conversion, an optical bandwidth of 0.78 nm, and an optical wavelength tuning range of 114 nm can be achieved in the *Z*-cut $LiNbO_3$ waveguide (*X*-propagation SAW at the acoustic center frequency of 607.4 MHz) at a guiding layer thickness of $0.6\ \mu$m, and an interaction length of 30 mm. An optical wavelength tuning range as large as 1300 nm is also achievable at the optical center wavelength of $1.55\ \mu$m, using a guiding layer thickness of $2.5\ \mu$m, in the *Z*-cut configuration. The corresponding acoustic drive power required at 100% $TM_0 \rightarrow TE_0$ mode conversion is 7.6 mW/mm at the acoustic center frequency of 142.7 MHz. For the AOTFs using the *X*-cut configuration together with the *Y*-propagation SAW, while the performance figures in terms of acoustic center frequency, optical bandwidth and optical wavelength tuning range do not differ significantly from those in the *Z*-cut configuration, the acoustic drive power density requirement is much higher than in the *Z*-cut configuration. For example, it is a factor of 10 and 25 higher at the optical center wavelength of $0.50\ \mu$m and $1.55\ \mu$m, respectively, with the corresponding guiding layer thickness of $0.6\ \mu$m and $2.5\ \mu$m.

Integrated AO Tunable Filters and Applications

Integrated AOTFs are well recognized to offer unique applications to spectroscopy, multispectral imaging, laser wavelength tuning, and fiber amplifier gain equalization, in addition to optical wavelength filtering and wavelength-division multiplexing and demultiplexing. As with the bulk-wave AOTFs, such integrated AOTFs possess the unique and desirable features of very large optical wavelength tuning range (from ultraviolet to far infrared), high resolution (up to subnanometer), high speed (up to submicrosecond), programmability, and relatively low RF drive power requirement. Furthermore, compared to the bulk-wave AOTFs, the integrated AOTFs have the added advantages of smaller size, lighter weight, higher degree of robustness, batch fabrication, and thus lower manufacturing cost.

BIBLIOGRAPHY

1. C. F. Quate, C. D. W. Wilkinson, and D. K. Winslow, Interaction of light and microwave sound, *Proc. IEEE,* **53**: 1604–1623, 1965.
2. A. J. DeMaria and G. E. Danielson, Jr., Internal laser modulation by acoustic lens-like effects, *IEEE J. Quantum Electron.,* **QE-2**: 157–164, 1996.
3. E. I. Gordon, A review of acoustooptical deflection and modulation, *Proc. IEEE,* **54**: 1391–1401, 1996.
4. R. Adler, Interactions of light and sound, *IEEE Spectrum,* **4**: 42, 1967.
5. R. W. Dixon, Acoustic diffraction of light in anisotropic media, *IEEE J. Quantum Electron.,* **QE-3**, 1967.

6. (a) R. W. Dixon, Photoelastic properties of selected materials and their relevance for applications to acoustic light modulators and scanners, *J. Appl. Phys.,* **38**: 5149–5153, 1967. (b) D. A. Pinnow, Guide lines for the selection of acoustooptic materials, *IEEE J. Quantum Electron.,* **QE-6**: 223–238, 1970.
7. (a) A. Korpel, Acousto-optics, in R. Wolfe (ed.), *Applied Solid-State Science,* New York: Academic, 1972, Vol. 3, Chap. 2, pp. 73–179; (b) A. Korpel, *Acousto-Optics,* 2nd ed., New York: Marcel Dekker, 1997; (c) P. Das and C. DeCusatis, *Acousto-Optic Signal Processing: Fundamentals & Applications,* Boston: Artech House, 1991; (d) A. Goutzoulis and D. Pape (eds.), *Design and Fabrication of Acousto-Optic Devices,* New York: Marcel Dekker, 1994; (e) T.-C. Poon, M. D. McNeill, and D. J. Moore, Modern optical signal processing experiments demonstrating intensity and pulse-width modulation using acousto-optic modulator, *Amer. J. Phys.,* **65**: 917–925, 1997.
8. (a) L. Kuhn et al., Deflection of an optical guided-wave by a surface acoustic wave, *Appl. Phys. Lett.,* **17**: 265–268, 1970; (b) Y. Ohmachi, Acousto-optical light diffraction in thin films, *J. Appl. Phys.,* **44**: 3928–3922, 1973.
9. (a) R. V. Schmidt and I. P. Kaminow, Acoustooptic Bragg deflection in $LiNbO_3$ Ti-diffused waveguides, *IEEE J. Quantum Electron.,* **QE-11**: 57–59, 1975; (b) C. S. Tsai et al., High-performance guided-light-beam device using two tilted surface acoustic wave, *Appl. Phys. Lett.,* **26**: 140–142, 1975.
10. (a) R. V. Schmidt, Acoustooptic interactions between guided optical waves and acoustic surface waves, *IEEE Trans. Sonics Ultrason.,* **SU-23**: 22–23, 1976; (b) I. C. Chang, Acoustooptic devices and applications, *IEEE Trans. Sonics Ultrason.,* **SU-23**: 2–22, 1976.
11. C. S. Tsai, Guided-wave acoustooptic Bragg modulators for wideband integrated optic communications and signal processing, *IEEE Trans. Circuits Syst.,* **CAS-26**: 1072–1089, 1979.
12. C. S. Tsai (ed.), *Guided-Wave Acoustooptic Bragg Diffraction, Devices, and Applications,* Berlin: Springer-Verlag, 1990.
13. (a) C. S. Tsai, Integrated acoustooptic circuits and applications, *IEEE Trans. Ultrasonics Ferroelectr. Freq. Control,* **39**: 529–554, 1992; (b) C. S. Tsai, Integrated acoustooptic and magnetooptic devices for optical information processing, *Proc. IEEE,* **84**: 853–869, 1996.
14. P. K. Tien, Light waves in thin films and integrated optics, *Appl. Opt.,* **10**: 2395–2413, 1971.
15. H. F. Taylor and A. Yariv, Guided-wave optics, *Proc. IEEE,* **62**: 1044–1060, 1974.
16. H. Kogelnik, An Introduction to Integrated Optics, *IEEE Trans. Microw. Theory Tech.,* **23**: 2–16, 1975.
17. P. K. Tien, Integrated optics and new wave phenomena in optical waveguides, *Rev. Mod. Phys.,* **49**: 361–423, 1977.
18. T. Tamir, Ed., *Integrated Optics,* Berlin: Springer-Verlag, 1979.
19. A. Yariv, *Introduction to Optical Electronics,* 2nd ed., New York: Holt, Rinehart and Winston, 1976.
20. (a) R. Hunsberger, *Integrated Optics: Theory and Technology,* Berlin: Springer-Verlag, 1982; (b) H. P. Nolting and R. Ulrich (ed.), *Integrated Optics,* Berlin: Springer-Verlag, 1985.
21. (a) R. M. White, Surface elastic waves, *Proc. IEEE,* **58**: 1238–1276, 1970; (b) G. W. Farnell, Properties of elastic surface waves, in W. P. Mason and R. N. Thurston (eds.), *Physical Acoustics,* Vol. 6, New York: Academic Press, 1970, pp. 109–166; (c) A. A. Oliner (Ed.), *Surface Acoustic Waves,* Berlin: Springer-Verlag, 1979; and (d) G. W. Farnell and E. L. Adler, Elastic wave propagation in thin layers, in W. P. Mason and R. N. Thurston (eds.), *Physical Acoustics,* Vol. 9, New York: Academic Press, 1972.
22. R. W. Smith et al., Design of surface wave delay lines with integrated transducers, *IEEE Trans. Microw. Theory Tech.,* **MTT-17**: 856–873, 1969.
23. G. S. Kino and R. S. Wagers, Theory of interdigital couplers on nonpiezoelectric substrates, *J. Appl. Phys.,* **44**: 1480–1488, 1973.
24. G. S. Kino, *Acoustic Waves: Devices, Imaging, and Analogy Signal Processing,* Englewood-Cliffs, NJ: Prentice-Hall, 1987.
25. D. A. Smith and Z. Bao, Technology and applications of the integrated acousto-optic filter, *Proc. MELECON 96,* IEEE, New York, 1997, pp. 100–107.
26. L. G. H. Lean, C. F. Quate, and H. J. Shaw, Continuous deflection of laser beams, *Appl. Phys. Lett.,* **10**: 48–51, 1967.
27. S. E. Harris and R. W. Wallace, Acousto-optic tunable filter, *J. Opt. Soc. Am.,* **59**: 744–747, 1969.
28. F. S. Hickernell and J. W. Brewer, Surface-elastic-wave properties of DC-triode-sputtered zinc oxide film, *Appl. Phys. Lett.,* **21**: 389–391, 1972.
29. (a) N. Chubachi, J. Kushibiki, and Y. Kikuchi, Monolithically integrated Bragg deflector for an optical guided wave made of zinc-oxide film, *Electron. Lett.,* **9**: 193–194, 1973. (b) N. Chubachi, ZnO films for surface acoustooptic devices on nonpiezoelectric substrates, *Proc. IEEE,* **64**: 772–774, 1976; (c) N. Chubachi and H. Sasaki, Surface acousto-optic interaction in ZnO thin films, *Wave Electron.,* **2**: 379, 1976.
30. R. V. Schmidt and I. P. Kaminow, Metal-diffused optical wave guides in $LiNbO_3$, *Appl. Phys. Lett.,* **25**: 459–460, 1974.
31. R. H. Tancrell and M. G. Holland, Acoustic surface wave filters, *Proc. IEEE,* **59**: 393–409, 1971.
32. W. R. Smith, H. M. Gerard, and W. R. Jones, Analysis and design of dispersive interdigital surface-wave transducers, *IEEE Trans. Microw. Theory Tech.,* **MMT-20**: 458–471, 1972.
33. D. Maydan, Acoustooptical pulse modulators, *IEEE J. Quantum Electron.,* **QE-6**: 15–24, 1970.
34. (a) D. Y. Zang and C. S. Tsai, Single-mode waveguide microlenses and microlens arrays fabrication using titanium indiffused proton exchange technique in $LiNbO_3$, *Appl. Phys. Let.,* **48**: 703–705, 1985; (b) D. Y. Zang and C. S. Tsai, Titanium-indiffused proton-exchanged waveguide lenses in $LiNbO_3$ for optical information processing, *Appl. Opt.,* **25**: 2264–2271, 1986.
35. T. Van Duzer, Lenses and graded films for focusing and guiding acoustic surface waves, *Proc. IEEE,* **58**: 1230–1237, 1970.
36. C. S. Tsai, B. Sun, and A. K. Roy, Guided-wave acoustooptic Bragg diffraction in indium gallium arsenide phosphide waveguides, *Appl. Phys. Lett.,* **70**: 3185–3187, 1997.
37. (a) D. Marcuse, TE modes of graded-index slab waveguides, *IEEE J. Quantum Electron.,* **QE-9**: 1000–1006, 1973; (b) E. M. Conwell, Modes in optical waveguides formed by diffusion, *Appl. Phys. Lett.,* **26**: 328–329, 1973; (c) P. K. Tien et al., Optical waveguide modes in single crystalline $LiNbO_3$–$LiTaO_3$ solid solution films, *Appl. Phys. Lett.,* **24**: 503–506, 1974.
38. H. Kogelnik, Theory of dielectric waveguides, in T. Tamir (ed.), *Integrated Optics,* Berlin: Springer-Verlag, 1975, chap. 2.
39. (a) D. Mergerian et al., Zinc oxide transducer array for integrated optics, *1978 Ultrason. Symp., Proc.,* IEEE Cat. No. 78-CH1344-ISU, pp. 64–69; (b) N. Mikoshiba, Guided-wave acoustooptic interactions in ZnO film on nonpiezoelectric substrates, in C. S. Tsai (ed.), *Guided-Wave Acoustooptic Bragg Diffraction, Devices, and Applications,* Berlin: Springer-Verlag, 1988, Chap. 6.
40. (a) A. Yariv and P. Yeh, *Optical Waves in Crystals,* New York: Wiley, 1984, chap. 11; (b) Y. Suematsu, Advances in semiconductor lasers, *Phys. Today,* **32**: 32–39, 1985.
41. (a) J. L. Merz, R. A. Logan, and A. M. Sergent, GaAs integrated optical circuits by wet chemical etching, *IEEE J. Quantum Electron.,* **QE-5**: 72–82, 1979; (b) N. Bar-Chaim et al., GaAs integrated optoelectronics, *IEEE Trans. Electron. Devices,* **ED-29**: 1372, 1982; (c) A. Yariv, The beginning of integrated optoelectronic circuits, *IEEE Trans. Electron. Devices,* **ED-3**: 1956, 1984;

(d) O. Wada, T. Sakurai, and T. Nakagami, Recent progress in optoelectronic integrated circuits, *IEEE J. Quantum Electron.,* **QE-22**: 805, 1986.

42. (a) C. J. Lii, C. S. Tsai, and C. C. Lee, Wideband guided-wave acoustooptic Bragg cells in GaAs–GaAlAs waveguide, *IEEE J. Quantum Electron.,* **QE-22**: 868–872, 1986; (b) Y. Abdelrazak and C. S. Tsai, High performance acoustooptic Bragg cells in ZnO–GaAs waveguide at GHz frequencies, *Optoelectronics-Devices and Technologies,* **4**: 33–37, 1989; (c) Y. Abdelrazek, C. S. Tsai, and T. Q. Vu, An integrated optic RF spectrum analyzers in ZnO–GaAs–AlGaAs waveguide, *IEEE Lightwave Tech.,* **8**: 1833–1837, 1990. (d) A. M. Matteo, V. M. N. Passaro, and M. N. Armenise, High-performance guided-wave acoustooptic Bragg cells in $LiNbO_3$ and GaAs-based structures, *IEEE Trans. Ultrason. Ferroelectr. Freq. Control.,* **43**: 270–279, 1996.
43. O. Yamazaki et al., Guided-wave acoustooptic interactions in GaAs–ZnO composite structure, *1982 IEEE Ultrason. Symp. Proc.,* IEEE Cat. No. 82CH1823-4, pp. 418–421.
44. T. L. Koch and U. Koren, Semiconductor photonic integrated circuits, *IEEE J. Quantum Electron.,* **QE-27**: 641–653, 1991.
45. (a) W. T. Tsang and A. Y. Cho, Molecular beam epitaxial writing of patterned GaAs epilayer structures, *Appl. Phys. Lett.,* **32**: 491–493, 1978; (b) R. D. Dupus and P. D. Dapkus, Preparation and properties of $GA_{1-x}Al_xAs$-GaAs heterostructures lasers grown by metalorganic chemical vapor deposition, *IEEE J. Quantum Electron.,* **QE-15**: 128, 1979.
46. C. S. Tsai, B. Sun, and A. Kar-Roy, Guided-wave acoustooptic Bragg diffraction in InGaAsP waveguides, *Appl. Phys. Lett.,* **70**: 3185–3187, 1997.
47. N. Suzuki and K. Tada, Elastooptic properties of InP, *Jpn. J. Appl. Phys.,* **22**: 441–445, 1983.
48. J. L. Jackel, C. E. Rice, and J. J. Veslka, Proton-exchange for high index waveguide in $LiNbO_3$, *Appl. Phys. Lett.,* **47**: 607, 1982.
49. M. DeMicheli et al., Fabrication and characterization of Titanium-Indiffused Proton Exchanged (TIPE) waveguide in lithium niobate, *Opt. Commun.,* **42**: 101, 1982.
50. (a) T. Q. Vu, J. A. Norris, and C. S. Tsai, Planar waveguide lenses in GaAs using ion milling, *Appl. Phys. Lett.,* **54**: 1098–1100, 1989; (b) J. M. Verdiell et al., Aspheric waveguide lenses for photonic integrated circuits, *Appl. Phys. Lett.,* **62**: 808–810, 1993; (c) T. J. Su and C. C. Lee, Planar fabrication process of a high coupling efficiency interface between optical waveguides of large index difference, *Appl. Opt.,* **34**: 5366–5374, 1995.
51. H. I. Smith, F. J. Bachner, and N. Efremow, A high-yield photolithographic technique for surface wave devices, *J. Electrochem. Soc.,* **118**: 822–825, 1971.
52. T. Q. Vu, C. S. Tsai, and Y. C. Kao, Integration of curved hybrid waveguide lens and photodetector array in a GaAs waveguide, *Appl. Opt.,* **31**: 5246–5254, 1992.
53. S. E. Harris and R. W. Wallace, Acoustooptic tunable filter, *J. Opt. Soc. Am.,* **59**: 744–749, 1969.
54. I. C. Chang, Noncollinear acoustooptic filter with large angular aperture, *Appl. Phys. Lett.,* **25**: 370–372, 1974.
55. Y. Omachi and J. Noda, $LiNbO_3$ TE-TM mode converter colinear acoustooptic interaction, *IEEE Quantum Electron.,* **OE-13**: 43–46, 1977.
56. B. Kim and C. S. Tsai, Thin film tunable optical filtering using anisotropic and noncollinear acoustooptic interaction in $LiNbO_3$ waveguides, *IEEE J. Quantum Electron.,* **QE-15**: 642–647, 1979.
57. J. Frangen et al., Integrated optical, acoustically tunable wavelength filter, *Electron. Lett.,* **25**: 1583–1584, 1989.
58. G. D. Boyd and F. Heismann, Tunable acoustooptic reflection filters in $LiNbO_3$ without a Doppler shift, *J. Lightwave Technol.,* **7**: 625–631, 1989.
59. D. A. Smith et al., Integrated optic acoustically tunable filters for WDM networks, *IEEE J. Sel. Areas Comm.,* **8**: 1151–1159, 1990.
60. D. A. Smith and J. J. Johnson, Low drive-power integrated acoustooptic filter on X-cut Y-cut propagating $LiNbO_3$, *IEEE Photon. Technol. Lett.,* **3**: 923–925, 1991.
61. Y. Yamamoto, C. S. Tsai, and K. Esteghamat, Guided-wave acoustooptic tunable filters using simple coupling weighting technique, *Proc. Ultrasonics Symp.,* New York: IEEE, 1990, pp. 605–608, (IEEE Catalogue no. 90CH2938-9); Also, Y. Yamamoto et al., Suppression of sidelobe levels for guided-wave acoustooptic tunable filters using weighted coupling, *IEEE Trans. Ultrason. Ferroelectr. Freq. Control,* **40**: 813–818, 1993.
62. A. Kar-Roy and C. S. Tsai, Integrated acoustooptical tunable filters using weighted coupling, *IEEE J. Quantum Electron.,* **30**: 1574–1586, 1994.
63. A. Kar-Roy and C. S. Tsai, Low sidelobe weighted-coupled integrated acoustooptic tunable filter using focused surface acoustic waves, *IEEE Photon. Technol. Lett.,* **4**: 1132–1135, 1992.
64. D. A. Smith and J. J. Johnson, Sidelobe suppression in an acoustooptic filter with raised-cosine interaction strength, *Appl. Phys. Lett.,* **61**: 1025–1027, 1992.
65. H. Hermann and S. Schmid, Integrated acoustooptical mode converters with weighted coupling using surface wave directional couplers, *Electron. Lett.,* **28**: 979–980, 1992.
66. A. Kar-Roy and C. S. Tsai, Ultralow sidelobe-level integrated acoustooptic tunable filters using tapered-gap surface acoustic wave directional couplers, *J. Lightwave Tech.,* **12**: 977–982, 1994.
67. W. R. Trunta, Jr., D. W. Dolfi, and C. A. Flory, Anomalous sidelobes and birefringence apodization in acoustooptic tunable filters, *Opt. Lett.,* **18**: 28–30, 1993.
68. B. L. Heffner et al., Integrated-optic acoustically tunable infrared optical filter, *Electron. Lett.,* **24**: 1562–1563, 1988.
69. I. Hinkov and H. Hinkov, Integrated acoustooptic collinear TE-TM mode converters for 0.8 μm optical wavelength range, *Electron. Lett.,* **27**: 1211–1213, 1991.
70. R. R. Weiss and T. K. Gaylord, Lithium niobate: Summary of physical properties and crystal structure, *J. Appl. Phys. A,* **37**: 191–203, 1985.
71. R. M. De La Rue, Materials for waveguide optoelectronics, in J. Marsh and R. M. De La Rue (eds.), *Waveguide Optoelectronics,* NATO ASI Series, Series E: Applied Sciences, Vol. 226, 1992.

CHEN S. TSAI
University of California